# Compact High-Order Gas-Kinetic Scheme for Three-Dimensional Flow Simulations

Xing Ji,* Fengxiang Zhao,† Wei Shyy,‡ and Kun Xu§
*The Hong Kong University of Science and Technology, Hong Kong Special Administrative Region, People's Republic of China*

**A third-order compact gas-kinetic scheme is proposed for three-dimensional compressible flow computations. The new scheme is based on three key ingredients: the time-accurate gas evolution model for interface flux, the Hermite weighted essentially nonoscillatory reconstruction, and the two-stage temporal discretization. In contrast to the Riemann-solver-based methods, due to the use of time-accurate flux function the proposed scheme can achieve a third-order temporal accuracy with two stages instead of three stages in the standard Runge–Kutta method. As an extension of the existing high-order reconstructions, a Hermite weighted essentially nonoscillatory reconstruction is specifically designed for the current scheme with the implementation of the constrained least-square technique, which subsequently improves the accuracy and robustness of the compact scheme. There is no trouble cell identification in the current scheme. A third-order accuracy can be achieved even with curved boundary. Numerical examples for both smooth and discontinuous flows show the robustness and high accuracy of the compact third-order scheme, which has a comparable performance as the fifth-order noncompact gas-kinetic scheme. A large Courant–Friedrichs–Lewy number around 0.5 can be used in the computations.**

## Nomenclature

| | | |
|---|---|---|
| $A$ | = | temporal derivative for the gas distribution function |
| $a_{x_i}$ | = | spatial derivative for the gas distribution function ($i$ is equal to 1, 2, 3) |
| $C_D$ | = | drag coefficient |
| $\boldsymbol{F}$ | = | fluxes for conservative variables |
| $f, g$ | = | gas distribution function |
| $K$ | = | the number of internal degree of freedoms |
| $\mathcal{L}$ | = | spatial operator |
| $Ma$ | = | Mach number |
| $Pr$ | = | Prandtl number |
| $p$ | = | pressure |
| $Re$ | = | Reynolds number |
| $S$ | = | entropy |
| $t$ | = | time |
| $\boldsymbol{U}, U, V, W$ | = | macroscopic velocity vector and each components |
| $\boldsymbol{u}$ | = | particle velocity |
| $\boldsymbol{W}$ | = | conservative variables |
| $\boldsymbol{x}$ | = | location in physical space |
| $\beta$ | = | smoothness indicator |
| $\gamma$ | = | specific heat ratio |
| $\delta$ | = | normalized nonlinear weight |
| $\mu$ | = | dynamic viscosity coefficient |
| $\xi$ | = | internal degree of freedom |
| $\rho$ | = | density |
| $\sigma$ | = | global smoothness indicator |
| $\tau$ | = | physical collision time |
| $\tau_n$ | = | numerical collision time |
| $\omega$ | = | nonlinear weight |

*Subscript*

| | | |
|---|---|---|
| $\infty$ | = | freestream |

*Postdoctoral Fellow, Department of Mathematics; xjiad@connect.ust.hk.
†Graduate Student, Department of Mechanical and Aerospace Engineering; fzhaoac@connect.ust.hk.
‡Chair Professor, Department of Mechanical and Aerospace Engineering; weishyy@ust.hk. Fellow AIAA.
§Chair Professor, Department of Mathematics and Department of Mechanical and Aerospace Engineering; also Shenzhen Research Institute; makxu@ust.hk.

## I. Introduction

TREMENDOUS efforts have been paid on the development of high-order computational fluid dynamics (CFD) methods for the compressible Euler and Navier–Stokes (N-S) equations in past decades. Representative methods include weighted essentially nonoscillatory (WENO) methods [1], discontinuous Galerkin (DG) methods [2], the flux reconstruction (FR) [3] or correction procedure via reconstruction (CPR) [4] methods, etc. WENO-type reconstruction has been widely applied on structured grids, which can keep good robustness with very high order of accuracy [5]. However, due to the use of large stencils it is not a trivial task to extend the WENO approach to unstructured mesh or nonuniform mesh with the high-order accuracy. A new class of WENO schemes has been proposed recently in the attempt of releasing the problems [6].

On the other hand, the development of high-order compact methods, which only involve the target cell and its von Neumann neighbors for the update of numerical solution, becomes a hot research project due to its attractive properties, such as the good mesh adaptability and scalability [7]. Two main representatives of compact methods are the DG methods with a combination of finite volume and finite element frameworks, and the FR/CPR methods with the hybridization of finite difference and finite volume discretization. These methods can achieve arbitrary high-order accuracy with compact stencil and have great mesh adaptability. Numerical results have demonstrated their performance in large-eddy simulation (LES) [8] and Reynolds-averaged Navier–Stokes calculations [9] for smooth flow. However, in the flow simulations with strong discontinuities, these methods seem lack of robustness. Many attempts have been used to modify the updates of the internal degrees of freedom [10]. At the same time, these methods have restricted time step in comparison with the traditional high-order finite volume methods. Progress has been made continuously in the development of high-order schemes, such as the recent multimoment constrained finite volume scheme [11], $P_N P_M$ scheme [12], and reconstructed-DG (rDG) method [13,14]. Most of these methods commonly use Riemann solvers or approximate Riemann solvers in the flux evaluation and the Runge–Kutta (RK) time-stepping methods for temporal accuracy.

A class of compact high-order gas-kinetic scheme (HGKS) has been developed recently [15]. With the use of the two-stage temporal

discretization [16,17], and the Hermite WENO (HWENO) reconstruction [18], a fourth-order compact gas-kinetic scheme (GKS) on two-dimensional (2-D) structured mesh is constructed [19]. The compact scheme has a higher resolution than the conventional noncompact fourth-order GKS [20] and has similar robustness as a second-order shock capturing scheme. Most importantly, a large Courant–Friedrichs–Lewy (CFL) number around 0.5 can be used in the computation. The success of the above fourth-order compact GKS lies in the following distinguishable features:

1) The GKS flux is based on an analytical integral solution of the kinetic model equation with a complete flow physics [21]. The time-dependent gas distribution function at a cell interface provides a multiple scale flow evolution from the kinetic particle transport to the hydrodynamic wave propagation, which bridges the approaches seamlessly between the kinetic flux vector splitting and the central difference Lax–Wendroff-type discretization.

2) Both inviscid and viscous fluxes are obtained from the moments of a single time-accurate gas distribution function, which has special advantages in the construction of the scheme on unstructured mesh.

3) The GKS is a multidimensional scheme [22], where both normal and tangential derivatives of flow variables around a cell interface contribute to the time evolution of the gas distribution function.

4) Besides fluxes, the time-accurate gas distribution function also provides time-evolving flow variables at each Gaussian point on the cell interface. Based on these time-accurate solutions at interfaces, the time-evolving derivatives of the flow variables in the cell can be evaluated as well through the Gauss's theorem. Therefore, the compact HWENO reconstruction can be adopted in the reconstruction. The update of the slopes in the compact GKS has fundamental differences from the updating methods in DG/CPR, where a weak formulation is directly obtained for the update of the corresponding degrees of freedom. The compact GKS updates the flow variables and the slopes based on the same gas evolution solution at cell interface, and it uses the same time step as a noncompact high-order finite volume scheme and keeps the same robustness in the discontinuous flow region.

5) The multistage multiderivative (MSMD) time discretization can be adopted due to the existence of the time derivative of the flux function in GKS. For the Riemann-solver-based methods, for the same time accuracy more stages in the RK method have to be used. With the strong stability preserving (SSP) property [23], the $N$th–order accuracy in RK methods requires no less than $N$ stages. For a classical fourth-order RK method, four stages are basically needed. Even though the evaluation of the GKS flux is more expensive than the time-independent Riemann solver, with the incorporation of the MSMD method, the fourth-order time accuracy can be achieved from two stages with a reduction of expensive reconstruction in comparison with RK method [20,24].

The compact GKS [19] has been developed up to eighth-order spatial accuracy in rectangular mesh [25], which has a spectral-like resolution at large wavenumber and has been successfully applied in the aeroacoustic problems with shock interaction [26]. The extension on triangular mesh [27] also demonstrates excellent robustness in the hypersonic flow computation. Thus, it becomes natural to develop three-dimensional (3-D) scheme for real engineering applications.

In this paper, a compact third-order GKS on 3-D multiblock structured mesh will be constructed under the same GKS framework [27,28]. In the general hexahedron mesh, different from the direction-by-direction reconstruction [25,28], multidimensional polynomials are directly constructed in a least-squares sense. In the constrained least-square approach, the cell-averaged values are exactly kept, which shows a favorable linear stability and accuracy for smooth flow. For structured mesh with curved boundary, the vertices of a hexahedral cell can become easily non-coplanar. To determine the location and normal direction at each Gaussian point uniquely, the trilinear/bilinear interpolation is used with the satisfaction of global mesh volume conservation. As a result, the scheme is able to keep the formal order of accuracy under nonuniform or curvilinear meshes. To deal with discontinuities, most effort has been paid on the spatial reconstruction. The traditional WENO reconstruction [18,29] requires a large number of substencils and may have nonpositive

weights on nonuniform mesh [30]. Recently, a new WENO method was proposed [31], of which the key idea is to construct a whole weighted polynomial in a cell rather than pointwise value at each Gaussian point. The linear weights can be chosen to be positive numbers with a summation of one and the expected order of accuracy can be kept in the smooth region. Moreover, the number of substencils is less than the conventional WENO method. In turn, efficiency and robustness are greatly improved in comparison with the traditional WENO. Following the idea in [31], a new HWENO-type reconstruction based on the cell-averaged values and the first-order derivatives is constructed for the initial condition. Different from the original approach [31] with the use of neighbor-to-neighbor cells in the stencils, the current reconstruction is designed on a compact stencil with von Neumann neighbors only and has a better parallelization capability. This compact reconstruction can be directly implemented on unstructured hexahedron grid. The new scheme inherits the advantages of the previous compact GKS [19,27]. In comparison with the third-order RK time-stepping method, the compact GKS achieves a third-order accuracy in time with one middle stage only. A CFL number of 0.5 can be taken safely in both smooth and discontinuous flow simulations, whereas the CFL number is on the order of 0.2 for a third-order DG method. The comparison of accuracy is given between the proposed compact scheme and the noncompact HGKS [24], which shows that the former one has superiority in the implicit LES simulations. The tests including hypersonic flow passing through a sphere also validate the robustness of the current compact GKS in 3-D structured mesh.

This paper is organized as follows. The basic framework for the 3-D compact high-order GKS is presented in Sec. II. In Sec. III, the general formulation for the two-stage high-order temporal discretization is introduced. In Sec. IV, the compact third-order HWENO reconstruction on hexahedral mesh is presented. Numerical experiments including inviscid and viscous tests are presented in Sec. V to validate the proposed scheme. The last section is the conclusion.

## II.   Compact Finite Volume Gas-Kinetic Scheme

The 3-D gas-kinetic Bhatnagar–Gross–Krook (BGK) equation [32] can be written as

$$f_t + \boldsymbol{u} \cdot \nabla f = \frac{g - f}{\tau} \tag{1}$$

where $f$ is the gas distribution function, $g$ is the corresponding equilibrium state, and $\tau$ is the collision time; $f = f(\boldsymbol{x}, t, \boldsymbol{u}, \xi)$, where $\boldsymbol{x}$ is location in physical space, $t$ is time, and $\boldsymbol{u}$ is particle velocity in phase space.

The collision term satisfies the following compatibility condition:

$$\int \frac{g - f}{\tau} \boldsymbol{\psi} \, \mathrm{d}\Xi = 0 \tag{2}$$

where $\boldsymbol{\psi} = (1, \boldsymbol{u}, (1/2)(\boldsymbol{u}^2 + \xi^2))^T$, $\mathrm{d}\Xi = \mathrm{d}u_1 \mathrm{d}u_2 \mathrm{d}u_3 \mathrm{d}\xi_1 \ldots \mathrm{d}\xi_K$, $K$ is the number of internal degree of freedoms (i.e., $K = (5 - 3\gamma)/(\gamma - 1)$ in 3-D case), and $\gamma$ is the specific heat ratio.

Based on the Chapman–Enskog expansion for BGK equation [33], the gas distribution function in the continuum regime can be expanded as

$$f = g - \tau D_{\boldsymbol{u}} g + \tau D_{\boldsymbol{u}} (\tau D_{\boldsymbol{u}}) g - \tau D_{\boldsymbol{u}} [\tau D_{\boldsymbol{u}} (\tau D_{\boldsymbol{u}}) g] + \ldots \tag{3}$$

where $D_{\boldsymbol{u}} = \partial/\partial t + \boldsymbol{u} \cdot \nabla$. By truncating on different orders of $\tau$, the corresponding macroscopic equations can be derived. If the zeroth-order truncation is taken, i.e., $f = g$, the Euler equations can be recovered by taking moments of $\boldsymbol{\psi}$ on Eq. (1):

$$\boldsymbol{W}_t + \nabla \cdot \boldsymbol{F}(\boldsymbol{W}) = 0$$

With the first-order truncated distribution function,

$$f = g - \tau (\boldsymbol{u} \cdot \nabla g + g_t) \tag{4}$$

the N-S equations can be obtained:

$$W_t + \nabla \cdot F(W, \nabla W) = 0$$

with $\mu = \tau p$ and unit Prandtl number.

Based on the time-dependent distribution function $f$, the macroscopic conservative variables are

$$W(x, t) = \int \psi f(x, t, u, \xi) \, d\Xi \tag{5}$$

and the corresponding fluxes $F(W(x, t))$,

$$F(x, t) = \int u \psi f(x, t, u, \xi) \, d\Xi \tag{6}$$

For a finite volume scheme, the cell-averaged conservative variables are updated through the interface fluxes. Besides the fluxes, the time-accurate cell interface gas distribution function also provides flow variables through Eq. (5) at the next time level, and subsequently determines the cell averaged slopes. The update of cell interface value $W(x, t)$ requires a high-order gas evolution model with time-accurate interface solution, which cannot be achieved by the first-order Riemann solver.

### A. Finite Volume Scheme on General Structured Mesh

For a polyhedron cell $\Omega_i$ in 3-D space, the boundary can be expressed as

$$\partial \Omega_i = \bigcup_{p=1}^{N_f} \Gamma_{ip}$$

where $N_f$ is the number of cell interfaces for cell $\Omega_i$, e.g., $N_f = 4$ for tetrahedron and $N_f = 6$ for cuboid or general hexahedron.

The increment of the cell averaged conservative flow variables in a finite control volume $i$ in a time interval $[t_n, t_{n+1}]$ can be expressed as

$$W_i^{n+1} |\Omega_i| = W_i^n |\Omega_i| - \sum_{p=1}^{N_f} \int_{\Gamma_{ip}} \int_{t_n}^{t_{n+1}} F(x, t) \cdot n_p \, dt \, ds \tag{7}$$

with

$$F(x, t) \cdot n_p = \int \psi f(x, t, u, \xi) u \cdot n_p \, d\Xi \tag{8}$$

where $W_i$ is the cell averaged value over cell $\Omega_i$, $|\Omega_i|$ is the volume of $\Omega_i$, $F$ is the interface flux, and $n_p = (n_1, n_2, n_3)^T$ is the unit vector representing the outer normal direction of $\Gamma_{ip}$. The semidiscretized form of finite volume scheme can be written as

$$\frac{dW_i}{dt} = \mathcal{L}(W_i) = -\frac{1}{|\Omega_i|} \sum_{p=1}^{N_f} \int_{\Gamma_{ip}} F(W) \cdot n_p \, ds \tag{9}$$

Numerical quadratures can be adopted to give a high-order spatial approximation for $F_{ip}(t)$, where Eq. (7) can be rewritten as

$$W_i^{n+1} |\Omega_i| = W_i^n |\Omega_i| - \sum_{p=1}^{N_f} |\Gamma_{ip}| \sum_{k=1}^{M} \omega_k \int_{t_n}^{t_{n+1}} F(x_{p,k}, t) \cdot n_p \, dt \tag{10}$$

The bilinear interpolation is used to describe a given quadrilateral interface $\Gamma_{ip}$ with coplanar or non-coplanar vertices. $M = 2 \times 2$ Gaussian points are used to meet the requirement of a third-order spatial accuracy. In the computation, the fluxes are obtained under the local coordinates. Details can be found in [34].

### B. Gas-Kinetic Solver

To construct the numerical fluxes at the Gaussian point $x = (0, 0, 0)^T$, the integral solution of BGK equation (1) is used:

$$f(x, t, u, \xi) = \frac{1}{\tau} \int_0^t g(x', t', u, \xi) e^{-(t-t')/\tau} \, dt' + e^{-t/\tau} f_0(x - ut, u, \xi) \tag{11}$$

where $x = x' + u(t - t')$ is the trajectory of particle, $f_0$ is the initial gas distribution function, and $g$ is the corresponding equilibrium state. The integral solution states a physical process from the particle free transport in $f_0$ in the kinetic scale to the hydrodynamic flow evolution in the integration of $g$ term. The flow evolution at the cell interface depends on the ratio of time step to the local particle collision time $\Delta t/\tau$. We refer [33] for the detailed construction of the gas-kinetic flux function. In short, the second-order time-dependent gas distribution function is given as

$$\begin{aligned} f(0, t, u, \xi) = & (1 - e^{-t/\tau_n}) g^c + [(t + \tau) e^{-t/\tau_n} - \tau] a_{x_i}^c u_i g^c \\ & + (t - \tau + \tau e^{-t/\tau_n}) A^c g^c \\ & + e^{-t/\tau_n} g^l [1 - (\tau + t) a_{x_i}^l u_i - \tau A^l] H(u_1) \\ & + e^{-t/\tau_n} g^r [1 - (\tau + t) a_{x_i}^r u_i - \tau A^r](1 - H(u_1)) \end{aligned} \tag{12}$$

where $\tau_n$ is the numerical collision time $\tau_n$, which will be defined later; $g^{l,r}$ can be fully determined from the reconstructed macroscopic variables $W^l, W^r$ at the left and right sides of a cell interface:

$$\int \psi g^l \, d\Xi = W^l, \quad \int \psi g^r \, d\Xi = W^r \tag{13}$$

Similarly, $W^c$ are the macroscopic flow variables for the determination of the equilibrium state $g^c$:

$$\int \psi g^c \, d\Xi = W^c$$

The microscopic coefficients can be determined by the spatial derivatives of macroscopic flow variables and the compatibility condition as follows:

$$\langle a_{x_1} \rangle = \frac{\partial W}{\partial x_1} = W_{x_1}, \quad \langle a_{x_2} \rangle = \frac{\partial W}{\partial x_2} = W_{x_2}, \quad \langle a_{x_3} \rangle = \frac{\partial W}{\partial x_3} = W_{x_3},$$
$$\langle A + a_{x_1} u_1 + a_{x_2} u_2 + a_{x_3} u_3 \rangle = 0 \tag{14}$$

where $\langle \ldots \rangle$ are the moments of a gas distribution function defined by

$$\langle (\ldots) \rangle = \int \psi (\ldots) g \, d\Xi$$

The details for calculation of each microscopic term from macroscopic quantities can be found in [33].

For smooth flow, the time-dependent solution in Eq. (12) can be simplified as [21]

$$f(0, t, u, \xi) = g^c - \tau (a_{x_i}^c u_i + A^c) g^c + A^c g^c t \tag{15}$$

under the assumptions of continuous functions $g^{l,r} = g^c$, $a_{x_i}^{l,r} = a_{x_i}^c$. The above gas-kinetic solver for smooth flow has less numerical dissipations than the full GKS solver in Eq. (12) with the consideration of discontinuous initial data.

### C. Direct Evolution of the Cell Averaged First-Order Spatial Derivatives

Distinguished from the schemes based on the Riemann solvers, the gas-kinetic scheme provides a time evolution solution. Recalling Eq. (5), the conservative variables at the Gaussian point $x_{p,k}$ can be updated by taking moments $\psi$ on the interface gas distribution function in Eq. (12):

$$W_{p,k}(t^{n+1}) = \int \psi f^n(x_{p,k}, t^{n+1}, u, \xi) \, \mathrm{d}\Xi, \qquad k = 1, \dots, M \quad (16)$$

According to the Gauss's theorem, the cell-averaged first-order derivatives within each element at $t^{n+1}$ can be obtained by

$$
\begin{aligned}
\bar{W}_x^{n+1} &= \int_V \nabla \cdot (\bar{W}(t^{n+1}), 0, 0) \, \mathrm{d}V = \frac{1}{\Delta V} \int_{\partial V} (1, 0, 0) \cdot n \bar{W}(t^{n+1}) \, \mathrm{d}S \\
&= \frac{1}{\Delta V} \int_{\partial V} \bar{W}(t^{n+1}) n_1 \, \mathrm{d}S = \frac{1}{\Delta V} \sum_{p=1}^{N_f} \sum_{k=1}^{M} \omega_{p,k} W_{p,k}^{n+1}(n_1)_{p,k} \Delta S_p, \\
\bar{W}_y^{n+1} &= \int_V \nabla \cdot (0, \bar{W}(t^{n+1}), 0) \, \mathrm{d}V = \frac{1}{\Delta V} \int_{\partial V} (0, 1, 0) \cdot n \bar{W}(t^{n+1}) \, \mathrm{d}S \\
&= \frac{1}{\Delta V} \int_{\partial V} \bar{W}(t^{n+1}) n_2 \, \mathrm{d}S = \frac{1}{\Delta V} \sum_{p=1}^{N_f} \sum_{k=1}^{M} \omega_{p,k} W_{p,k}^{n+1}(n_2)_{p,k} \Delta S_p, \\
\bar{W}_z^{n+1} &= \int_V \nabla \cdot (0, 0, \bar{W}(t^{n+1})) \, \mathrm{d}V = \frac{1}{\Delta V} \int_{\partial V} (0, 0, 1) \cdot n \bar{W}(t^{n+1}) \, \mathrm{d}S \\
&= \frac{1}{\Delta V} \int_{\partial V} \bar{W}(t^{n+1}) n_3 \, \mathrm{d}S = \frac{1}{\Delta V} \sum_{p=1}^{N_f} \sum_{k=1}^{M} \omega_{p,k} W_{p,k}^{n+1}(n_3)_{p,k} \Delta S_p
\end{aligned}
$$
$$(17)$$

where $n_{p,k} = ((n_1)_{mp,k}, (n_2)_{p,k}, (n_3)_{p,k})$ is the outer unit normal direction at each Gaussian point $x_{p,k}$.

## III.  Two-Stage Temporal Discretization

The two-stage fourth-order (S2O4) temporal discretization that has been adopted in the previous compact GKS on 2-D cases is implemented here [19,27]. Following the definition of Eq. (9), a fourth-order time-accurate solution for cell-averaged conservative flow variables $W_i$ is updated by

$$W_i^* = W_i^n + \frac{1}{2} \Delta t \mathcal{L}(W_i^n) + \frac{1}{8} \Delta t^2 \frac{\partial}{\partial t} \mathcal{L}(W_i^n),$$

$$W_i^{n+1} = W_i^n + \Delta t \mathcal{L}(W_i^n) + \frac{1}{6} \Delta t^2 \left( \frac{\partial}{\partial t} \mathcal{L}(W_i^n) + 2 \frac{\partial}{\partial t} \mathcal{L}(W_i^*) \right) \quad (18)$$

where $\mathcal{L}(W_i^n)$ and $(\partial/\partial t)\mathcal{L}(W_i^n)$ are

$$\mathcal{L}(W_i^n) = -\frac{1}{|\Omega_i|} \sum_{p=1}^{N_f} \sum_{k=1}^{M} \omega_{p,k} F(x_{p,k}, t_n) \cdot n_{p,k},$$

$$\frac{\partial}{\partial t} \mathcal{L}(W_i^n) = -\frac{1}{|\Omega_i|} \sum_{p=1}^{N_f} \sum_{k=1}^{M} \omega_{p,k} \partial_t F(x_{p,k}, t_n) \cdot n_{p,k},$$

$$\frac{\partial}{\partial t} \mathcal{L}(W_i^*) = -\frac{1}{|\Omega_i|} \sum_{p=1}^{N_f} \sum_{k=1}^{M} \omega_{p,k} \partial_t F(x_{p,k}, t_*) \cdot n_{p,k} \quad (19)$$

The proof for the fourth-order accuracy can be found in [16].

Based on the time-accurate flux function in Eq. (12), the numerical fluxes $F_{p,k}$ and their time derivatives $\partial_t F_{p,k}$ at $t_n$ and $t_* = t_n + \Delta t/2$ can be constructed. Details can be found in [27]. The S2O4 time integration meets the requirement of a third-order temporal accuracy for the current scheme with only two stages.

Similar to the two-stage temporal discretization in the flux evaluation [27], the time-dependent gas distribution function in Eq. (16) is updated by

$$f^* = f^n + \frac{1}{2} \Delta t f_t^n,$$

$$f^{n+1} = f^n + \Delta t f_t^* \quad (20)$$

## IV.  Compact HWENO Reconstruction

In this section, a newly designed compact HWENO-type reconstruction will be presented to construct the cell interface values and their first-order derivatives at each Gaussian point on both sides of a cell interface. Then, based on such an initial condition the time-dependent gas distribution function in Eq. (12) can be fully determined.

As a starting point of WENO reconstruction, a linear reconstruction will be presented first. For a piecewise smooth function $Q(x)$ ($Q$ can be conservative or characteristic variables) over cell $\Omega_0$, a polynomial $P^r(x)$ with degrees $r$ can be constructed to approximate $Q(x)$ as follows:

$$P^r(x) = Q(x) + O(\Delta h^{r+1})$$

where $\Delta h \sim |\Omega_0|^{1/3}$ is the equivalent cell size. To achieve a third-order accuracy and satisfy conservative property, the following quadratic polynomial over cell $\Omega_0$ is obtained:

$$P^2(x) = \bar{Q}_0 + \sum_{|k|=1}^{2} a_k p^k(x) \quad (21)$$

where $\bar{Q}_0$ is the cell averaged value of $Q(x)$ over cell $\Omega_0$, $k = (k_1, k_2, k_3)$, and $|k| = k_1 + k_2 + k_3$. The $p^k(x)$ are basis functions, which are given by

$$p^k(x) = x_1^{k_1} x_2^{k_2} x_3^{k_3} - \frac{1}{|\Omega_0|} \iiint_{\Omega_0} x_1^{k_1} x_2^{k_2} x_3^{k_3} \, \mathrm{d}V$$

The trilinear interpolation is used to describe a given hexahedron $\Omega_0$ with coplanar or non-coplanar vertices. Detail can be found in [34].

### A.  Large Stencil and Substencils

To reconstruct the quadratic polynomial $P^2(x)$ on $\Omega_0$, the large stencil for reconstruction includes $\Omega_0$ and all its von Neumann neighbors, i.e., $\Omega_m, m = 1, \dots, 6$, where the averages of $Q(x)$ and averaged derivatives of $Q(x)$ over each cell are known.

The following values are used to obtain $P^2(x)$:

1) Cell averages $\bar{Q}$ for cell 0, 1, 2, 3, 4, 5, 6

2) Cell averages of the $x$-direction partial derivative $\bar{Q}_{x_1}$ for cell 1, 2, 3, 4, 5, 6

3) Cell averages of the $y$-direction partial derivative $\bar{Q}_{x_2}$ for cell 1, 2, 3, 4, 5, 6

4) Cell averages of the $z$-direction partial derivative $\bar{Q}_{x_3}$ for cell 1, 2, 3, 4, 5, 6

The polynomial $P^2(x, y)$ is required to exactly satisfy

$$\iiint_{\Omega_m} P^2(x, y) \, \mathrm{d}V = \bar{Q}_m |\Omega_m| \quad (22)$$

where $\bar{Q}_m$ is the cell averaged value over $\Omega_m, m = 1, \dots, 6$. Then, the following conditions are imposed in a least-squares sense:

$$\iiint_{\Omega_m} \frac{\partial}{\partial x_1} P^2(x) \, \mathrm{d}V = (\bar{Q}_{x_1})_m |\Omega_m|,$$

$$\iiint_{\Omega_m} \frac{\partial}{\partial x_2} P^2(x) \, \mathrm{d}V = (\bar{Q}_{x_2})_m |\Omega_m|,$$

$$\iiint_{\Omega_m} \frac{\partial}{\partial x_3} P^2(x) \, \mathrm{d}V = (\bar{Q}_{x_3})_m |\Omega_m| \quad (23)$$

where $\bar{Q}_{x_i}, i = 1, 2, 3$ are the cell averaged directional derivatives over $\Omega_m$ in a global coordinate, respectively. On a regular mesh, the system has 24 independent equations. The constrained least-square method is used to solve the above linear system [35].

The constraints introduced in Eq. (22) can improve the linear stability of the reconstruction and reduce the numerical errors.

The information from the cell-averaged values takes up a high proportion. Under uniform mesh, the coefficients in Eq. (21) for cell $\Omega_{i,j,k}$ are given in the form

$$a_{1,0,0} = \frac{\bar{Q}_{i+1,j,k} - \bar{Q}_{i-1,j,k}}{2h},$$

$$a_{0,1,0} = \frac{\bar{Q}_{i,j+1,k} - \bar{Q}_{i,j-1,k}}{2h},$$

$$a_{0,0,1} = \frac{\bar{Q}_{i,j,k+1} - \bar{Q}_{i,j,k-1}}{2h},$$

$$a_{2,0,0} = \frac{\bar{Q}_{i+1,j,k} + \bar{Q}_{i-1,j,k} - 2\bar{Q}_{i,j,k}}{2\,h^2},$$

$$a_{0,2,0} = \frac{\bar{Q}_{i,j+1,k} + \bar{Q}_{i,j+1,k} - 2\bar{Q}_{i,j,k}}{2\,h^2},$$

$$a_{0,0,2} = \frac{\bar{Q}_{i,j,k+1} + \bar{Q}_{i,j+1,k-1} - 2\bar{Q}_{i,j,k}}{2\,h^2},$$

$$a_{1,1,0} = \frac{(\bar{Q}_{x_1})_{i,j+1,k} - (\bar{Q}_{x_1})_{i,j-1,k} + (\bar{Q}_{x_2})_{i+1,j,k} - (\bar{Q}_{x_2})_{i-1,j,k}}{4h},$$

$$a_{0,1,1} = \frac{(\bar{Q}_{x_2})_{i,j,k+1} - (\bar{Q}_{x_2})_{i,j,k-1} + (\bar{Q}_{x_3})_{i,j+1,k} - (\bar{Q}_{x_3})_{i,j-1,k}}{4h},$$

$$a_{1,0,1} = \frac{(\bar{Q}_{x_1})_{i,j,k+1} - (\bar{Q}_{x_1})_{i,j,k-1} + (\bar{Q}_{x_3})_{i+1,j,k} - (\bar{Q}_{x_3})_{i-1,j,k}}{4h}$$

The information from the derivatives only shows in the cross terms. In addition, it will reduce to a third-order scheme involving the cell-averaged values only in the 1-D case.

To deal with discontinuity, eight substencils $S_j, j = 1, \ldots, 8$, are selected from the large one given in Fig. 1. The following cell averaged values for each substencil are used to get the linear polynomial $P_j^1(\boldsymbol{x})$:

$P_1^1$ on $S_1 = \{\bar{Q}_0, \bar{Q}_1, \bar{Q}_3, \bar{Q}_5\}$, $\quad$ $P_2^1$ on $S_2 = \{\bar{Q}_0, \bar{Q}_3, \bar{Q}_5, \bar{Q}_2\}$,

$P_3^1$ on $S_3 = \{\bar{Q}_0, \bar{Q}_5, \bar{Q}_2, \bar{Q}_4\}$, $\quad$ $P_4^1$ on $S_4 = \{\bar{Q}_0, \bar{Q}_4, \bar{Q}_2, \bar{Q}_6\}$,

$P_5^1$ on $S_5 = \{\bar{Q}_0, \bar{Q}_2, \bar{Q}_6, \bar{Q}_3\}$, $\quad$ $P_6^1$ on $S_6 = \{\bar{Q}_0, \bar{Q}_6, \bar{Q}_3, \bar{Q}_1\}$,

$P_7^1$ on $S_7 = \{\bar{Q}_0, \bar{Q}_6, \bar{Q}_4, \bar{Q}_1\}$, $\quad$ $P_7^1$ on $S_7 = \{\bar{Q}_0, \bar{Q}_4, \bar{Q}_1, \bar{Q}_5\}$

There is always one substencil in smooth region with the appearance of discontinuity near any one of the interfaces of the target cell. The method in [30] can be used to obtain $P_j^1(x, y)$, which avoids the singularity caused by mesh irregularity, and the linear polynomial is expressed as
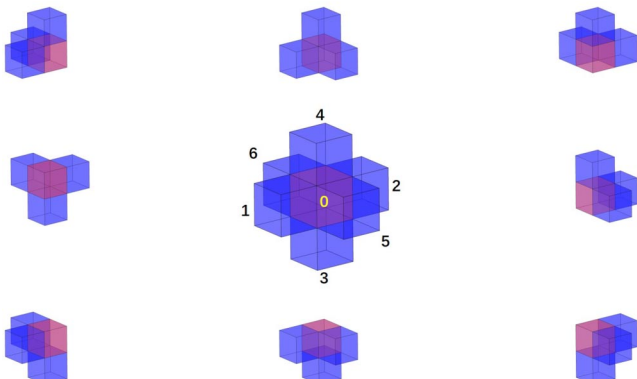


**Fig. 1** **The compact stencils of cell $\boldsymbol{\Omega_0}$ for HWENO-type reconstruction. Center: the large stencil. Others: the eight substencils.**

$$P_j^1(\boldsymbol{x}) = \bar{Q}_0 + \sum_{|k|=1}^1 a_{j,k} p^k(\boldsymbol{x}) \qquad (24)$$

Note that the choice of the large and substencils is not unique.

**B. Define the Values of Linear Weights**

$P^2(\boldsymbol{x})$ is written as

$$P^2(\boldsymbol{x}) = d_0\left[\frac{1}{d_0} P^2(\boldsymbol{x}) - \sum_{j=1}^8 \frac{d_j}{d_0} P_j^1(\boldsymbol{x})\right] + \sum_{j=1}^8 d_j P_j^1(\boldsymbol{x}) \qquad (25)$$

where the linear weights are chosen as $\gamma_0 = 0.92, \gamma_j = 0.01$, $j = 1, \ldots, 8$, according to [27,31].

**C. Compute the Nonlinear Weights**

The smoothness indicators $\beta_j, j = 0, \ldots, 8$, are defined as

$$\beta_j = \sum_{|\alpha|=1}^{r_j} |\Omega|^{(2/3)|\alpha|-1} \iiint_\Omega (D^\alpha P_j(\boldsymbol{x}))^2 \, \mathrm{d}V$$

where $\alpha$ is a multi-index and $D$ is the derivative operator, $r_0 = 2$, $r_j = 1, j = 1, \ldots, 8$. The smoothness indicators in Taylor series at $(x_0, y_0)$ have the order

$$\beta_0 = O\{|\Omega_0|^{2/3}[1 + O(|\Omega_0|^{2/3})]\} = O(|\Omega_0|)^{2/3} = O(h^2),$$

$$\beta_j = O\{|\Omega_0|^{2/3}[1 + O(|\Omega_0|^{1/3})]\} = O(|\Omega_0|)^{2/3} = O(h^2), \quad j = 1, \ldots, 8$$

By using a similar technique [31], a global smoothness indicator $\sigma$ can be defined:

$$\sigma = \left(\frac{1}{8}\sum_1^8 |\beta_0 - \beta_j|\right)^2 = O(|\Omega_0|^2) = O(h^6)$$

then the corresponding nonlinear weights are given by

$$\omega_j = d_j\left(1 + \frac{\sigma}{\epsilon + \beta_j}\right), \qquad j = 0, \ldots, 8,$$

$$\delta_j = \frac{\omega_j}{\sum_{l=0}^8 \omega_l} = d_j + O(h^4) \qquad (26)$$

where $\epsilon$ takes $10^{-8}$ to avoid zero in the denominator.

The final reconstruction polynomial for the approximation of $Q(\boldsymbol{x})$ yields

$$R(\boldsymbol{x}) = \delta_0\left[\frac{1}{d_0} P^2(\boldsymbol{x}) - \sum_{j=1}^8 \frac{d_j}{d_0} P_j^1(\boldsymbol{x})\right] + \sum_{j=1}^8 \delta_j P_j^1(\boldsymbol{x}) \qquad (27)$$

As a result, the nonlinear reconstruction achieves a third-order accuracy $R(\boldsymbol{x}) = Q(\boldsymbol{x}) + O(h^3)$. If any of these values yields negative density or pressure, the first-order reconstruction is used instead. So all the desired quantities at Gaussian points can be fully determined as

$$Q_{p,k}^{l,r} = R^{l,r}(\boldsymbol{x}_{p,k}), \quad (Q_{x_i}^{l,r})_{p,k} = \frac{\partial R^{l,r}}{\partial x_i}(\boldsymbol{x}_{p,k})$$

**D. Reconstruction of the Equilibrium State**

The reconstructions for the nonequilibrium states have the uniform order and can be used to get the equilibrium state directly, such as $g^c, g_{x_i}^c$ from a suitable averaging of $g^{l,r}, g_{x_i}^{l,r}$. The simplest way is to use the arithmetic average, but it is only applicable for smooth flow. To be consistent with the construction of $g^c$, we make an analogy of the kinetic-based weighting method for $g_{x_i}^c$, which are given by
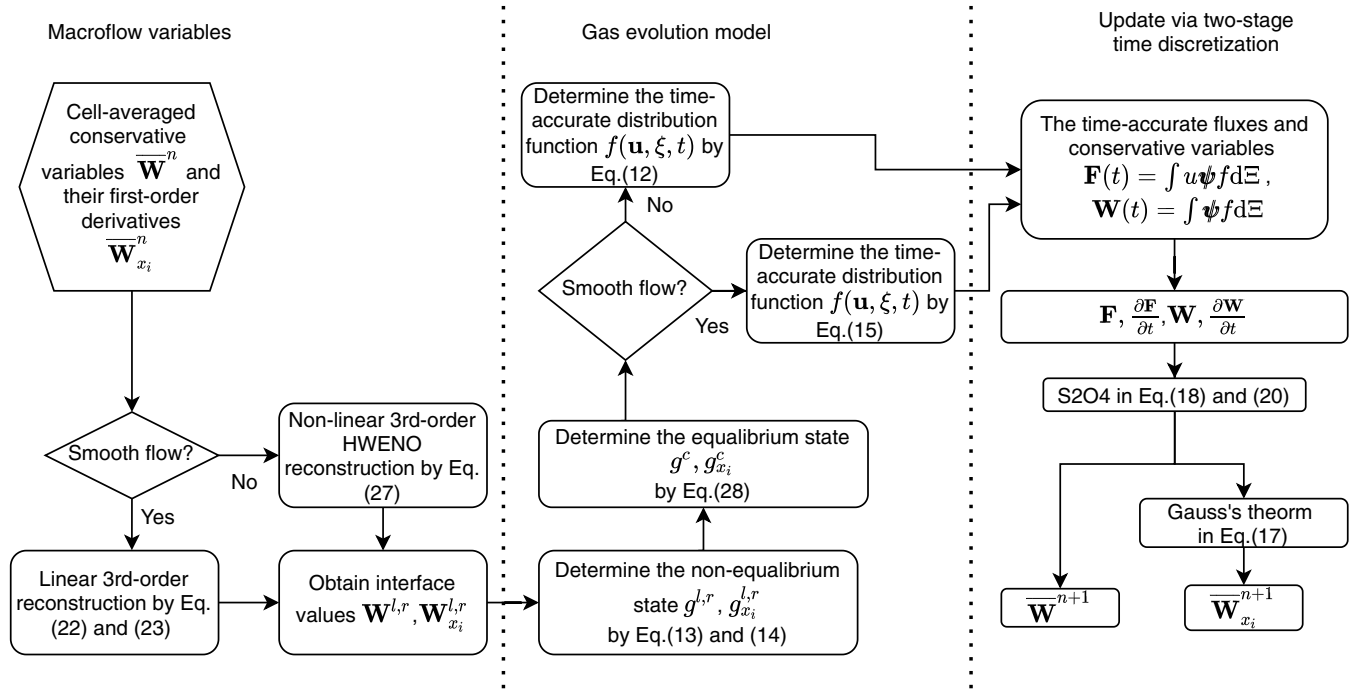
**Fig. 2   The brief algorithm of the compact GKS.**

$$\int \boldsymbol{\psi} g^c \, d\Xi = W^c = \int_{u>0} \boldsymbol{\psi} g^l \, d\Xi + \int_{u<0} \boldsymbol{\psi} g^r \, d\Xi,$$

$$\int \boldsymbol{\psi} g_{x_i}^c \, d\Xi = W_{x_i}^c = \int_{u>0} \boldsymbol{\psi} g_{x_i}^l \, d\Xi + \int_{u<0} \boldsymbol{\psi} g_{x_i}^r \, d\Xi \qquad (28)$$

This method has been validated in the noncompact WENO5-GKS [24]. In this way, all components of the microscopic slopes in Eq. (12) have been fully obtained.

Finally, a summary of the solution procedure is given in Fig. 2.

## V.   Numerical Tests

In this section, numerical tests will be presented to validate the compact high-order GKS. For the inviscid flow, the collision time is defined by

$$\tau = 0$$

and

$$\tau_n = \varepsilon \Delta t + C \left| \frac{p_l - p_r}{p_l + p_r} \right| \Delta t$$

where $\varepsilon = 0.01$ and $C = 1$. For the viscous flow, the collision time is related to the viscosity coefficient,

$$\tau = \frac{\mu}{p}$$

and

$$\tau_n = \frac{\mu}{p} + C \left| \frac{p_l - p_r}{p_l + p_r} \right| \Delta t$$

where $p_l$ and $p_r$ denote the pressure on the left and right sides of the cell interface, $\mu$ is the dynamic viscosity coefficient, and $p$ is the pressure at the cell interface. In smooth flow region, it reduces to $\tau_n = \tau = \mu/p$. The ratio of specific heats takes $\gamma = 1.4$. The inclusion of the pressure jump term is to enlarge the collision time in the discontinuous region, where the numerical cell size is not enough to resolve the shock structure. It increases the nonequilibrium transport mechanism in the flux function to mimic the physical process in the shock layer.

All reconstructions will be performed on the characteristic variables. Ghost cells are mainly adopted in the current scheme for boundary treatment. After obtaining the inner state at the boundary, a ghost state can be assigned according to boundary condition, and the corresponding gas distribution function in Eq. (12) can be determined. A high-order boundary reconstruction is only applied to the test of subsonic flow passing through a circular cylinder. The time step is determined by

$$\Delta t = C_{\text{CFL}} \text{Min} \left( \frac{\Delta r_i}{\|U_i\| + (a_s)_i}, \frac{(\Delta r_i)^2}{3 \nu_i} \right)$$

where $C_{\text{CFL}}$ is the CFL number, and $\|U_i\|$, $(a_s)_i$, and $\nu_i = (\mu/\rho)_i$ are the magnitude of velocities, sound speed, and kinematic viscosity coefficient for cell $i$. The $\Delta r_i$ is taken as

$$\Delta r_i = \frac{|\Omega_i|}{\text{Max} |\Gamma_{ip}|}$$

The CFL number is set as 0.5 if no specified in the test cases.

### A.   Accuracy Test

*1.   Three-Dimensional Sinusoidal Wave Propagation*

The advection of density perturbation is tested, and the initial condition is given as follows:

$$\rho(x, y, z) = 1 + 0.2 \sin(\pi(x + y + z)),$$

$$U(x, y, z) = (1, 1, 1), \quad p(x, y, z) = 1$$

within a cubic domain $[0, 2] \times [0, 2] \times [0, 2]$. In the computation, a series of uniform meshes with $N^3$ cells are used. With the periodic boundary condition in all directions, the analytic solution is

$$\rho(x, y, z, t) = 1 + 0.2 \sin(\pi(x + y + z - t)),$$

$$U(x, y, z) = (1, 1, 1), \quad p(x, y, z, t) = 1$$

The collision time $\tau = 0$ is set since the flow is smooth and inviscid. The $CFL = 0.5$ is used for computation. The $L^1$, $L^2$, and $L^\infty$ errors and the corresponding orders with linear and nonlinear $Z$-type weights at $t = 2$ are given in Tables 1 and 2. The expected accuracy is confirmed.

**Table 1    Accuracy test for the 3-D sine-wave propagation by the linear third-order compact reconstruction (CFL = 0.5)**

| Mesh number | $L^1$ error | Order | $L^2$ error | Order | $L^\infty$ error | Order |
|---|---|---|---|---|---|---|
| $5^3$ | 8.591164e-02 | — — | 9.529661e-02 | — — | 1.327066e-01 | — — |
| $10^3$ | 2.201313e-02 | 1.96 | 2.442492e-02 | 1.96 | 3.422233e-02 | 1.96 |
| $20^3$ | 3.084179e-03 | 2.84 | 3.432916e-03 | 2.83 | 5.054260e-03 | 2.76 |
| $40^3$ | 3.949479e-04 | 2.97 | 4.378248e-04 | 2.97 | 6.582257e-04 | 2.94 |
| $80^3$ | 4.954332e-05 | 2.99 | 5.490190e-05 | 3.00 | 8.289161e-05 | 2.99 |

**Table 2    Accuracy test for the 3-D sine-wave propagation by the nonlinear third-order compact HWENO reconstruction with $d_0 = 0.92$, $d_i = 0.01$, $i = 1,\ldots,8$ (CFL = 0.5)**

| Mesh number | $L^1$ error | Order | $L^2$ error | Order | $L^\infty$ error | Order |
|---|---|---|---|---|---|---|
| $5^3$ | 8.428434e-02 | — — | 9.425905e-02 | — — | 1.299919e-01 | — — |
| $10^3$ | 2.532893e-02 | 1.73 | 2.806704e-02 | 1.75 | 4.319655e-02 | 1.59 |
| $20^3$ | 3.113958e-03 | 3.02 | 3.595147e-03 | 2.96 | 6.419271e-03 | 2.75 |
| $40^3$ | 3.949729e-04 | 2.98 | 4.378852e-04 | 3.04 | 6.576984e-04 | 3.29 |
| $80^3$ | 4.954332e-05 | 2.99 | 5.490190e-05 | 3.00 | 8.289162e-05 | 2.99 |

The Riemann-solver-based finite volume schemes with high-order WENO reconstruction are widely used for compressible flow computations. To compare the efficiency between the Riemann-solver-based finite volume schemes and the current one, the following settings are adopted for conventional WENO methods:

1) For the Riemann-solver-based schemes, the noncompact third-order WENO reconstruction is applied. The reconstruction is performed on a direction-by-direction strategy [36], which is stable and efficient on structured mesh. The WENO weights are set as close as the current HWENO reconstruction according to [5,6]. One large stencil with $p^2$ polynomial and two substencils with $p^1$ polynomials are adopted. Their linear weights are set as 0.85, 0.075, and 0.075 as suggested in [5]. The nonlinear weights are chosen as the same formulation as that in Eq. (26), with the global smooth indicator $\theta = \left( (1/2) \sum_{j=1}^{2} |\beta_{p^2} - \beta_{j,p^1}| \right)^2$.

2) Two representative approximate Riemann solvers are used, i.e., the Lax–Friedrichs (LF) flux and the HLLC flux. The LF flux is very efficient but dissipative. The HLLC flux makes a good balance between the robustness and accuracy [37].

3) The widely used three-stage third-order RK method with strong stability property (RK3-SSP) is adopted [38].

4) Both algorithms are developed in the same in-house C++ code.

5) Both linear reconstruction and nonlinear WENO reconstruction are tested to evaluate the performance of the scheme under smooth flow and flow with discontinuities. For linear reconstruction, the gas-kinetic solver is simplified as that in Eq. (15).

A single core of Intel Xeon E5 2630v4 @2.20 GHz is used for all simulations. The CPU time and $L^1$ errors are recorded with mesh number from $5^3$ to $40^3$, as shown in Fig. 3. Under both cases, the RK3-LF scheme shows the poorest efficiency. The compact GKS with S2O4 time integration is around 37% faster than the RK3-HLLC scheme with nonlinear WENO reconstruction on characteristic variables. The difference becomes even larger when linear reconstruction is adopted, where the GKS is about 63% faster than the RK3-HLLC scheme.

Note that even for the current 3-D inviscid flow test, the GKS always solves the N-S equations. If RK3 Riemann-solver-based scheme is extended to solve the N-S equations, additional 17–20% computational cost is needed according to our test.

##### 2.    Subsonic Flow Past a Circular Cylinder

This 2-D test has been widely used to test the spatial accuracy of a high-order scheme with curved wall boundary [39–41]. A circular cylinder is put in the center of the computational domain with a radius of $r_0 = 0.5$. The computational domain is bounded by a concentric circle with radius $r_{out} = 20$. Four successively refined meshes with $16 \times 4 \times 4$, $32 \times 8 \times 4$, $64 \times 16 \times 4$, and $128 \times 32 \times 4$ cells are given according to [39]. Mesh distributions are shown in Fig. 4. The
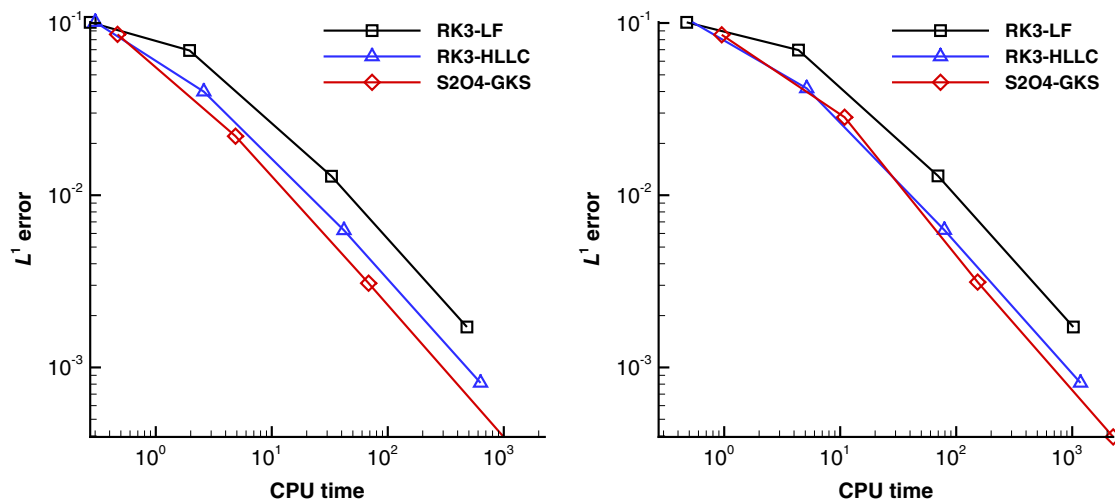
**Fig. 3    CPU time (in seconds) vs $L^1$ errors. Left: linear reconstruction based on conservative variables is adopted. Right: nonlinear reconstruction based on characteristic variables is adopted.**
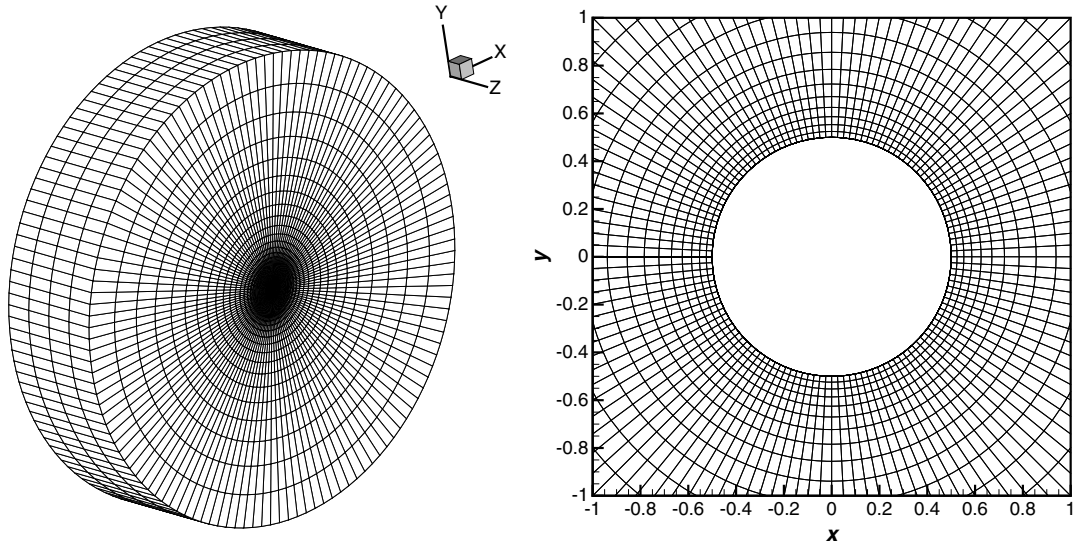
**Fig. 4    The mesh sample with $128 \times 32 \times 4$ cells for inviscid flow passing through a 3-D circular cylinder.**

reflective boundary condition is imposed on the wall of the cylinder. The far-field boundary at the outside of the domain has a freestream condition

$$(\rho, U, V, W, p)_\infty = \left(1, 0.38, 0, 0, \frac{1}{\gamma}\right)$$

with $\gamma = 1.4$. The periodic boundary condition is given in the $Z$ direction. It describes a subsonic inviscid flow at $Ma_\infty = 0.38$ passing through a cylinder. Ideally, the flow is isentropic with

$$S(x, y, t) = S_\infty$$

**Table 3    Accuracy test for subsonic flow passing through a circular cylinder**

| Mesh number | Second order | | Third order | |
|---|---|---|---|---|
| | $L^2$ error | Order | $L^2$ error | Order |
| $64 \times 16$ | 1.15e-03 | —— | 1.40e-4 | —— |
| $128 \times 32$ | 5.02e-5 | 4.51 | 1.01e-5 | 3.79 |
| $256 \times 64$ | 8.75e-6 | 2.52 | 1.19e-6 | 3.21 |

The curved boundary treatment is applied in both cases.

Thus, an entropy error, defined by

$$\epsilon_s = \frac{S - S_\infty}{S_\infty} = \frac{p}{p_\infty}\left(\frac{\rho_\infty}{\rho}\right)^\gamma - 1$$

is used for measuring the error of the numerical solution. The simulation is initialized with the freestream condition. The error is recorded when the flow gets to a steady state. To achieve a third-order accuracy on the cylindrical wall, a one-side compact stencil with six cells, $0, 1, \ldots, 5$, is used to reconstruct a smooth polynomial within a boundary cell 0. This stencil includes 21 data:

1) Cell averages $\bar{W}$ for cell 0, 1, 2, 3, 4, 5
2) Cell averages of the $x$-direction partial derivative $\bar{W}_x$ for cell 0, 1, 2, 3, 4, 5
3) Cell averages of the $y$-direction partial derivative $\bar{W}_y$ for cell 0, 1, 2, 3, 4, 5
4) Cell averages of the $z$-direction partial derivative $\bar{W}_z$ for cell 0, 1, 2, 3, 4, 5

A quadratic polynomial can be determined in a least-squares sense. Moreover, the normal direction at Gaussian point on the boundary is adjusted as that proposed in [39]. A third-order convergence rate is achieved through the above treatments, as shown in Table 3. The numerical result with low-order boundary reconstruction has a more visible wake than that with the high-order one, as shown in Fig. 5, where 20 equidistant Mach contours from 0.038 to 0.76 are plotted.
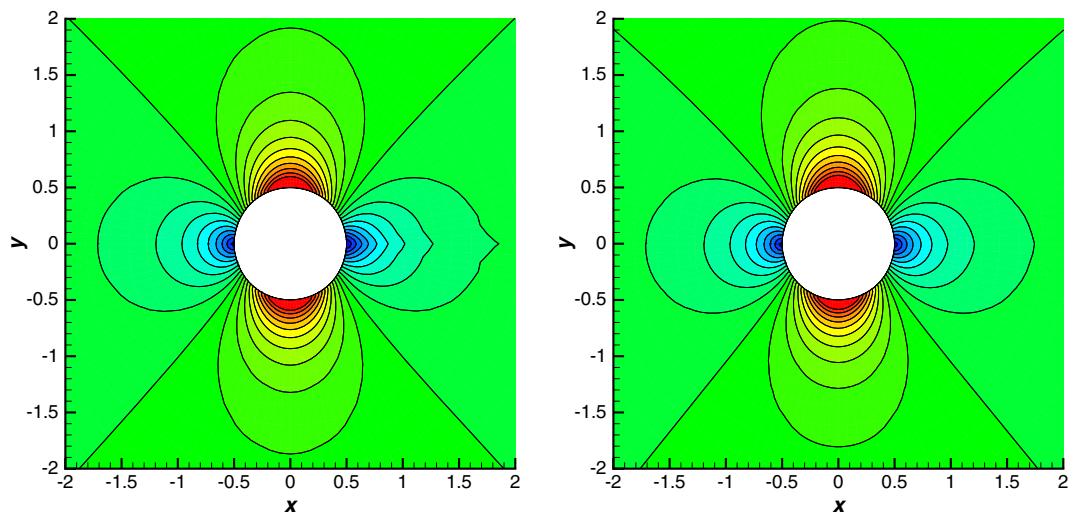


**Fig. 5    Subsonic flow passing through a circular cylinder. Mesh $128 \times 32 \times 4$. Left: the second-order boundary reconstruction. Right: the third-order compact boundary reconstruction. The curved boundary treatment is applied in both cases.**
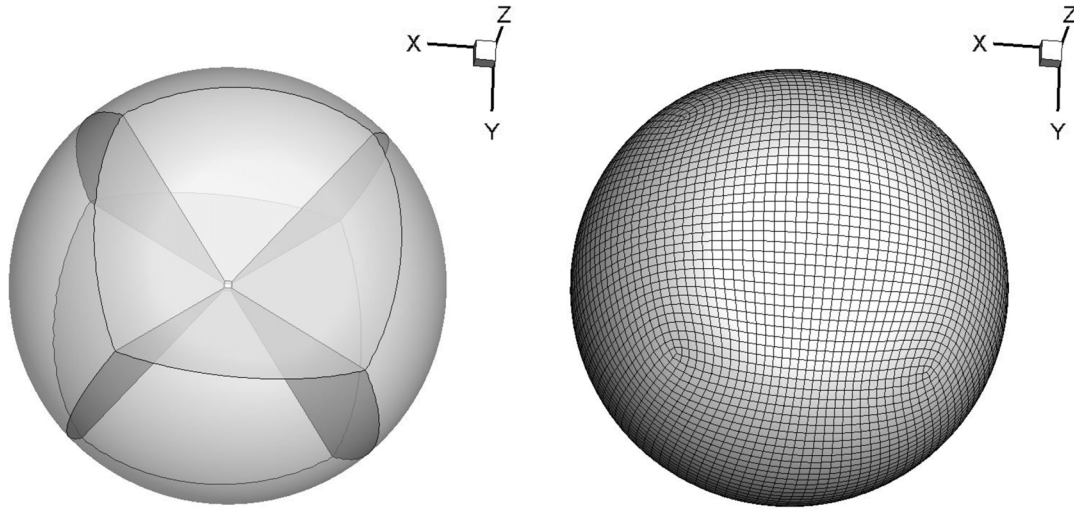
Fig. 6   The mesh for viscous flow passing through a sphere with $32 \times 32 \times 32 \times 6$ cells.

## B.   Subsonic Viscous Flow Passing Through a Sphere at $Re = 118$

This case is used to test the capability of the proposed method in resolving low-speed viscous flow. The Reynolds number based on the diameter of the sphere is 118. In such case, the drag coefficient $C_D = 1$ according to the experimental work [42].

The far-field boundary condition is set around the outside of the domain, which has a freestream condition

$$(\rho, U, V, W, p)_\infty = \left(1, 0.2535, 0, 0, \frac{1}{\gamma}\right)$$

with $\gamma = 1.4$ and $Ma_\infty = 0.2535$. The nonslip adiabatic boundary condition is imposed on the surface of the sphere. The structured grids with six blocks are used in the computation, as shown in Fig. 6. The diameter of the sphere is $D = 1$ and the grid size of the first cell above the wall is $2.45 \times 10^{-2} D$. The height of the grid grows from the wall with a constant ratio and stop at $20D$ in the radial direction. The shape of the steady separation bubble agrees well with each other. Table 4 shows the drag coefficient $C_D$, the separation angle $\theta$, and the closed wake length $L$ from the experiments and other computations. The drag coefficient is defined as

$$C_d = \frac{F_D}{(1/2)\rho_\infty U_\infty^2 S}$$

where $S = (1/4)\pi D^2$. The definition of $\theta$ and $L$ is given in Fig. 7. With similar degree of freedoms, the current compact GKS has the closest drag coefficient to the experiment data. The wake length has a visible difference from the experiment, but gets very close to DG's result [43]. The computational streamlines are compared with the experimental 4 streamlines [42] in Fig. 8.

Table 4   Comparisons among different schemes for the flow passing through a sphere

| Scheme | Degree of freedom | $C_d$ | $\theta$ | $L$ |
|---|---|---|---|---|
| Experiment [42] | — — | 1.0 | 151 | 1.07 |
| Current | 786,432 | 1.009 | 125.1 | 0.95 |
| Implicit third-order DDG [43] | 1,608,680 | 1.016 | 123.7 | 0.96 |
| Implicit fourth-order VFV [44] | 458,915 | 1.014 | — — | — — |
| Implicit third-order AMR-VFV [45] | 621,440 | 1.016 | — — | — — |
| Fourth-order FR [46] | — — | — — | 123.6 | 1.04 |

DDG = direct DG, VFV = variational-reconstruction finite volume method, and AMR = adaptive mesh refinement.
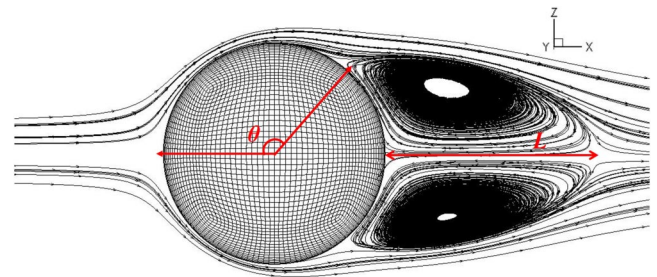


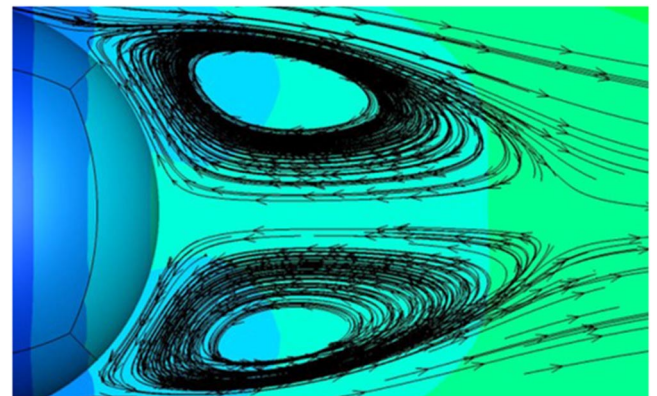Fig. 7   The definition of the separation angle $\theta$ and the closed wake length $L$.



Fig. 8   Comparison of streamlines between the experiment and computation. Reprinted in part with permission from [42]. © (1956) The Physical Society of Japan.

## C. Taylor–Green Vortex

The implicit large-eddy simulation (ILES) of a 3-D Taylor–Green vortex [47] is conducted to validate the new compact GKS for nearly incompressible viscous flow. The initial condition can be found in [24]. The specific heat ratio $\gamma = 1.4$ and the Prandtl number is $Pr = 1$. Two Reynolds numbers $Re = 280$ and $1600$ are studied here. The linear weights of reconstruction and the smooth flux function in Eq. (15) are adopted in this case. The equilibrium state is obtained by the arithmetic average of the nonequilibrium states to further reduce the numerical dissipations. The CFL is set as 0.3. Two time dependent variables are investigated in the current study. The first one is the volume-averaged kinetic energy

$$E_k = \frac{1}{\rho_0 \Omega} \int_\Omega \frac{1}{2} \rho U \cdot U \, d\Omega$$

where $\Omega$ is the volume of the computational domain. The second one is the dissipation rate of the kinetic energy

$$\varepsilon_k = -\frac{dE_k}{dt}$$

which is obtained through a second-order interpolation from the data $E_k(t_i)$, $t_i \in [0, t_{\text{stop}}]$,

$$\varepsilon_k(t_i) = -\frac{E_k(t_{i+1}) - E_k(t_{i-1})}{t_{i+1} - t_{i-1}}$$

The numerical results are compared with the reference direct numerical simulation data in [47] and the noncompact fifth-order GKS [24]. The isosurfaces of $Q$ criterion colored by Mach number at $t = 5$ and 10 for $Re = 1600$ case are shown in Fig. 9. With the time increment, the vortex structures become denser and smaller. The case with high Reynolds number has a rich flow structures, which requires high-resolution computation.

For $Re = 280$, the quantitative result agrees with the reference data under a coarse mesh $96^3$, as shown in Fig. 10. The new third-order compact GKS even shows better accuracy than the traditional fifth-order GKS with the same mesh points, as shown in Fig. 10c. The time history of the normalized volume-averaged kinetic energy and dissipation rate under $Re = 1600$ with $128^3$ and $196^3$ mesh points are presented in Fig. 11. The zoom-in plots are given in Fig. 12. Compact GKS is able to capture the complicated vortex structure as the noncompact one under the same mesh.

The computational cost on a single core of Intel Xeon E5 2630v4 @2.20 GHz is compared for the current compact GKS on a domain with $128^3$ mesh points. For the update of a single time step, the noncompact fifth-order GKS uses 113.93 s, whereas the compact GKS uses 106.6 s.

## D. Three-Dimensional Explosion Test

As an extension of the Sod problem, the spherical explosion test is considered. The initial condition is given by

$$(\rho, U, V, W, p) = \begin{cases} (1, 0, 0, 0, 1), & 0 < r < 0.5, \\ (0.125, 0, 0, 0, 0.1), & 0.5 \le r < 1 \end{cases}$$
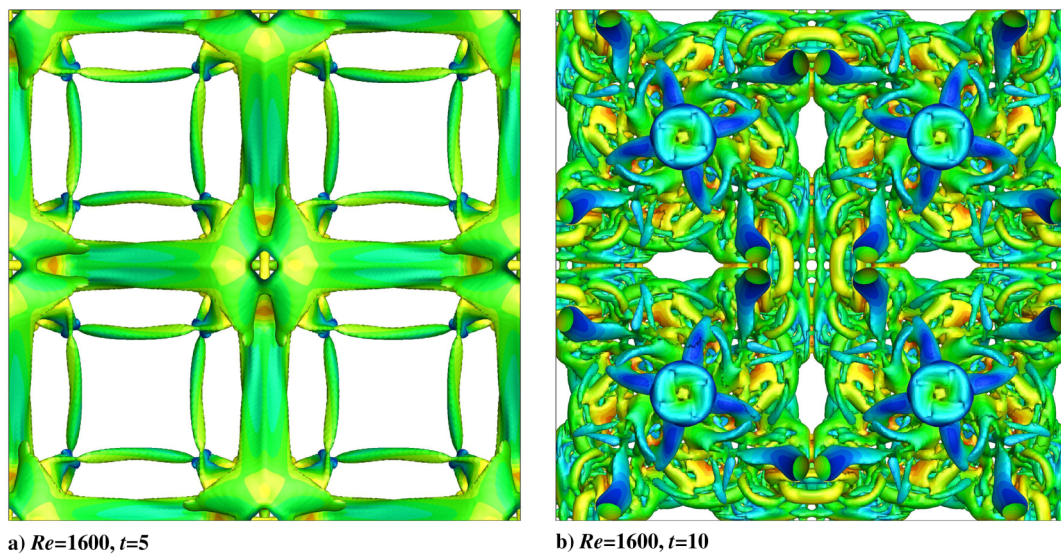


a) $Re=1600, t=5$        b) $Re=1600, t=10$

**Fig. 9** Taylor–Green vortex: the isosurfaces of $Q$ criterion colored by Mach number at time $t = 5$ and 10 for $Re = 1600$. Cell number $= 196^3$. The $x$–$y$ plane is shown.



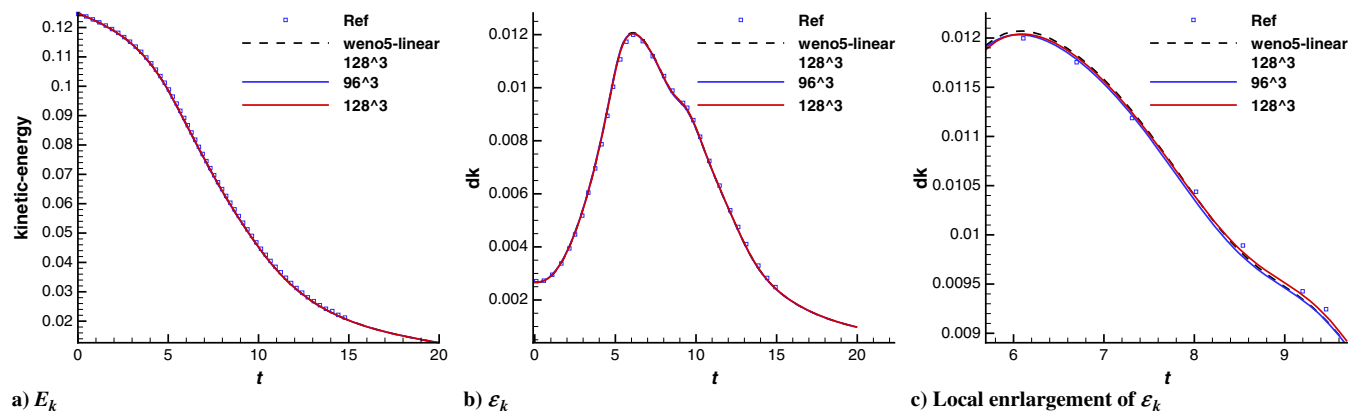a) $E_k$        b) $\varepsilon_k$        c) Local enlargement of $\varepsilon_k$

**Fig. 10** Taylor–Green vortex: $Re = 280$. The time history of kinetic energy and its dissipation rate.
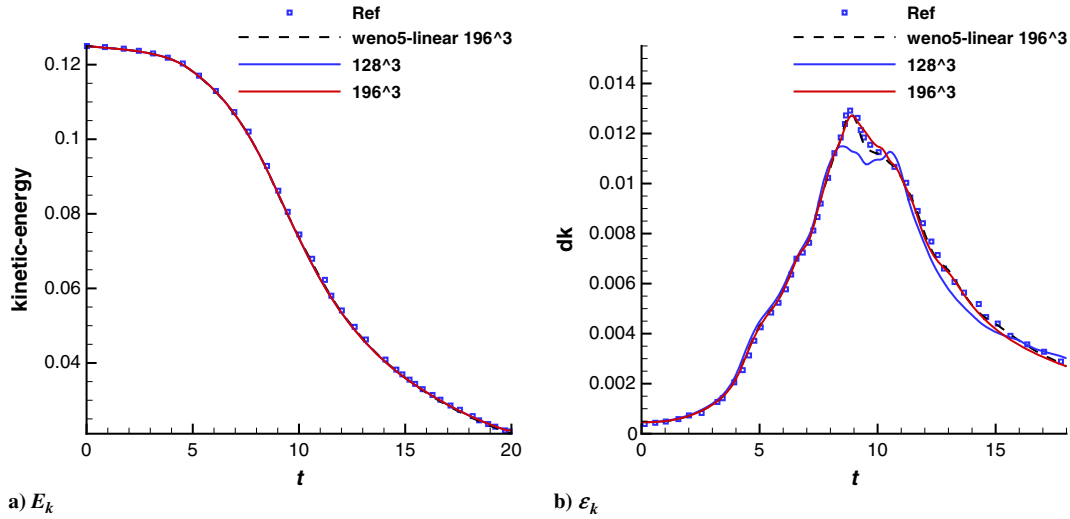
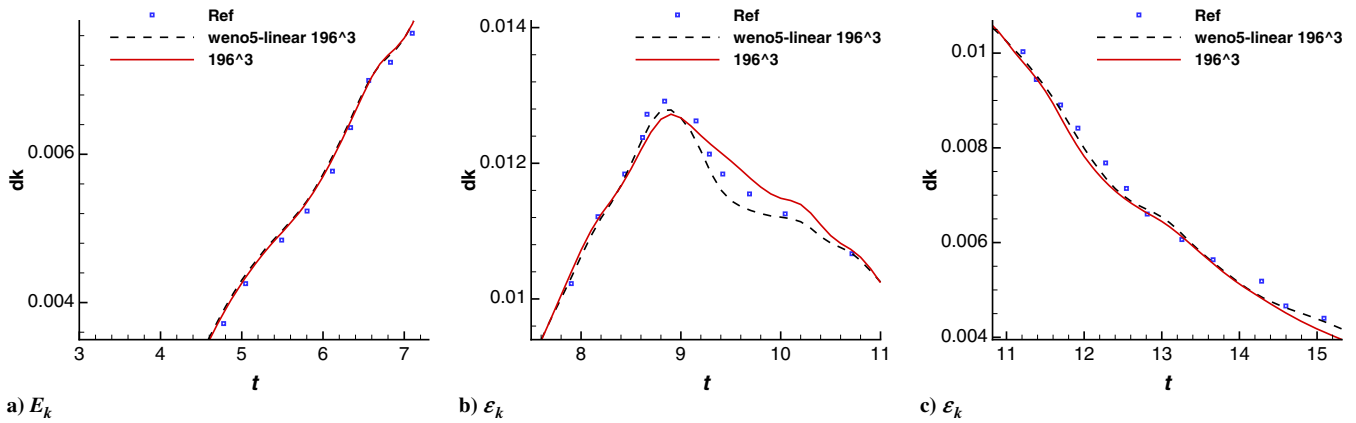**Fig. 11    Taylor–Green vortex: $Re = 1600$. The time history of kinetic energy and its dissipation rate.**



**Fig. 12    Taylor–Green vortex: $Re = 1600$. The local enlargement of the time history of kinetic energy dissipation rate.**

where $r = \sqrt{(x^2 + y^2 + z^2)}$. The solution contains a spherical shock wave and a contact surface traveling away from the center and a spherical rarefaction wave moving toward the origin $(0, 0, 0)$. To save the computational cost, the computation is on a domain $(x, y, z) \in [0, 1] \times [0, 1] \times [0, 1]$ covered by a uniform mesh $dx = dy = dz = 1/100$. The symmetric boundary conditions are imposed on the planes $x = 0$, $y = 0$, and $z = 0$, whereas the outflow boundary conditions are imposed on the planes $x = 1$, $y = 1$, $z = 1$. The density and pressure profiles along different radial directions at $t = 0.25$ are given in Fig. 13. The compact GKS resolves the wave

profiles crisply. Slightly overshoot can be observed at the front of the rarefaction wave.

### E.    High-Speed Flow Passing Through a Sphere

To validate the robustness of the current scheme with non-coplanar meshes, high-speed flow pasting through a sphere is tested. The structured grids with six blocks are used in the computation. A mesh sample is shown in Fig. 14. The diameter of the sphere is $D = 1$. Both inviscid and viscous flows are tested with a $CFL = 0.5$.
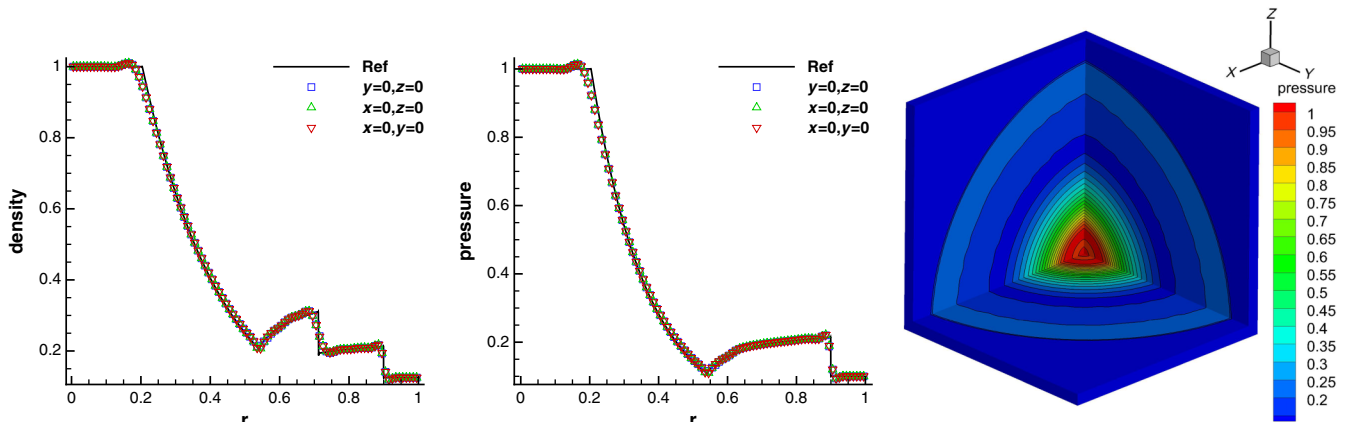


**Fig. 13    Three-dimensional explosion problem with $100^3$ cells. Left and middle: the density and pressure profiles extracted along the lines of $(y = 0, z = 0)$, $(x = 0, z = 0)$, and $(x = 0, y = 0)$. Right: 3-D view of pressure distribution.**
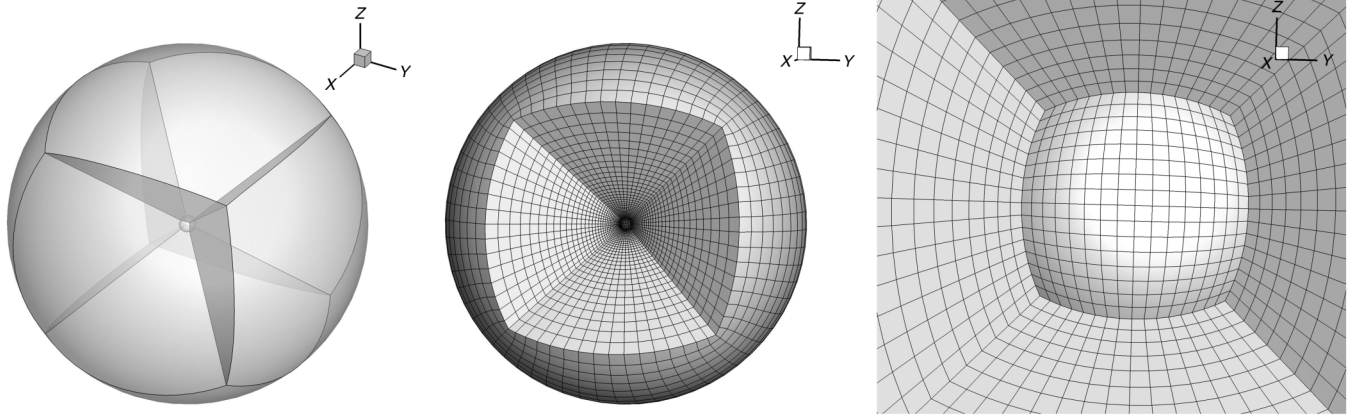
**Fig. 14  The mesh for supersonic viscous flow passing through a sphere with $16 \times 16 \times 32 \times 6$ cells.**

For the inviscid case, the slip boundary condition is imposed on the surface of the sphere. The first grid off the wall is $1 \times 10^{-2}D$. The outer domain is around $3.75D$ in the radial direction. The total cell number is $32 \times 32 \times 50 \times 6 = 307{,}200$. The supersonic inlet/outlet is adopted on the outside boundary, which is set according to the angle between the outer-pointing normal vector of each boundary interface and the incoming velocity. A supersonic flow with $Ma = 3$ is tested first. The simulation starts with the freestreaming flow condition. The pressure and Mach distributions at steady state are shown in Fig. 15. The maximum Mach number in the whole domain
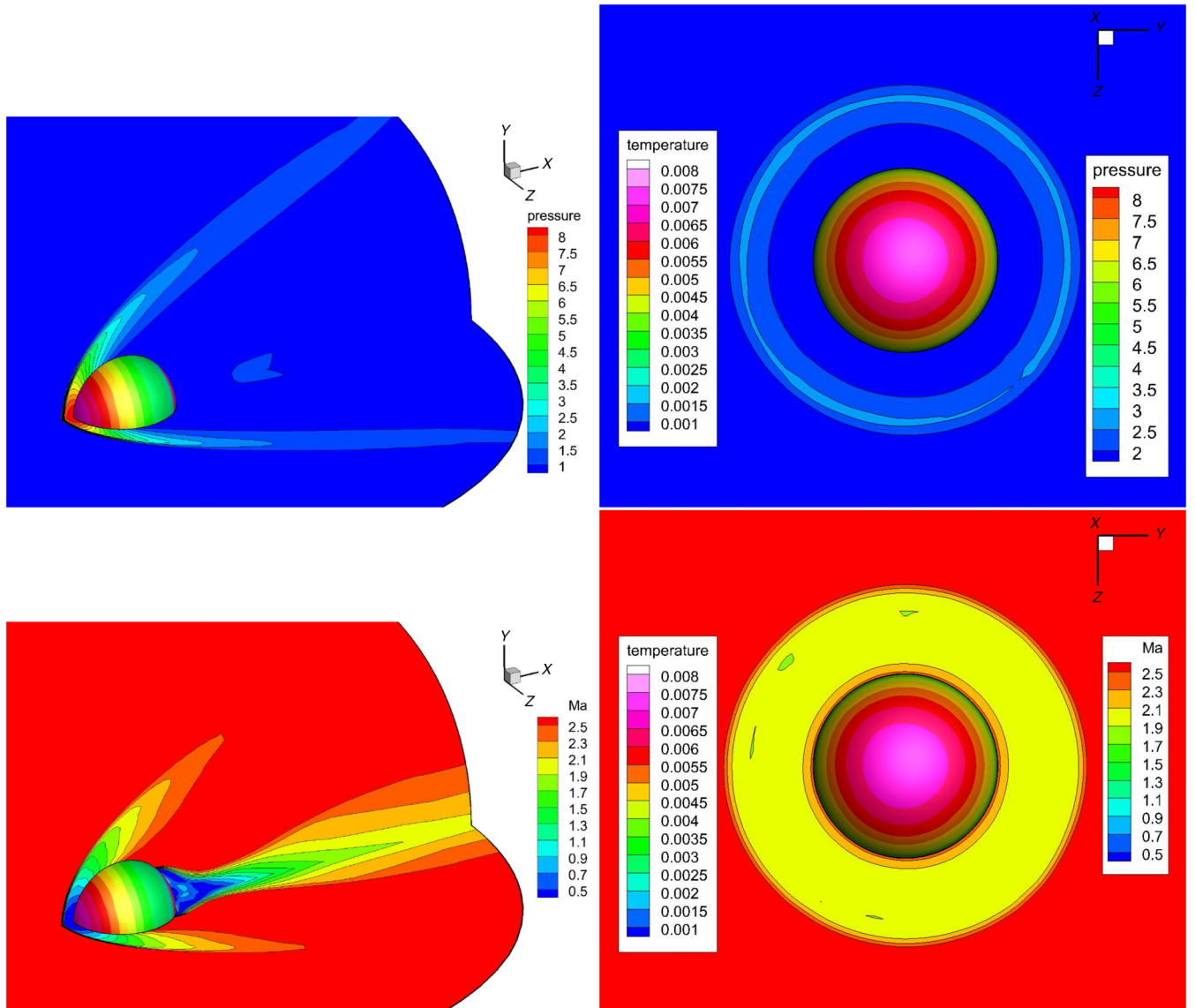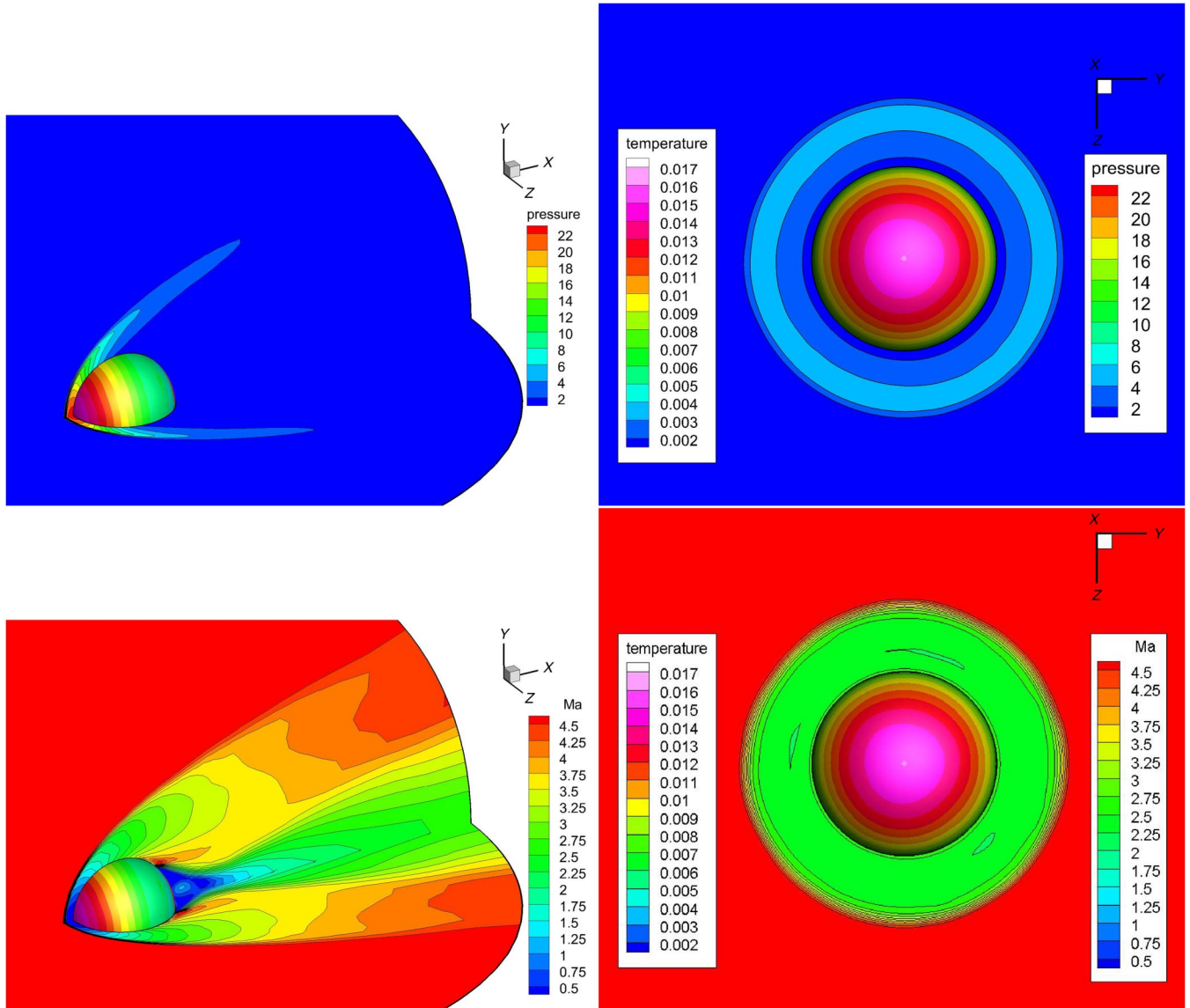


**Fig. 15  The pressure and Mach distributions of the supersonic inviscid flow passing through a sphere at $Ma = 3$. Left: $x$–$y$ and $x$–$z$ planes. Right: $y$–$z$ plane. The sphere is colored by the temperature.**

Fig. 16 The pressure and Mach distributions of the hypersonic inviscid flow passing through a sphere at $Ma = 5$. Left: $x$–$y$ and $x$–$z$ planes. Right: $y$–$z$ plane. The sphere is colored by the temperature.

is about 5.5. Then, hypersonic flow with $Ma = 5$ is tested. A primary flowfield calculated by the first-order kinetic method [33] is used as the initial field. The numerical results are shown in Fig. 16. The maximum Mach number $Ma_{\text{Max}} \approx 7.3$ is observed in the whole

domain. The shock is captured sharply and the carbuncle phenomenon does not appear in both cases. The result is essentially axisymmetric. The asymmetric pattern can be observed at the leeward side of the sphere. A nearly vacuum state forms in this region and the
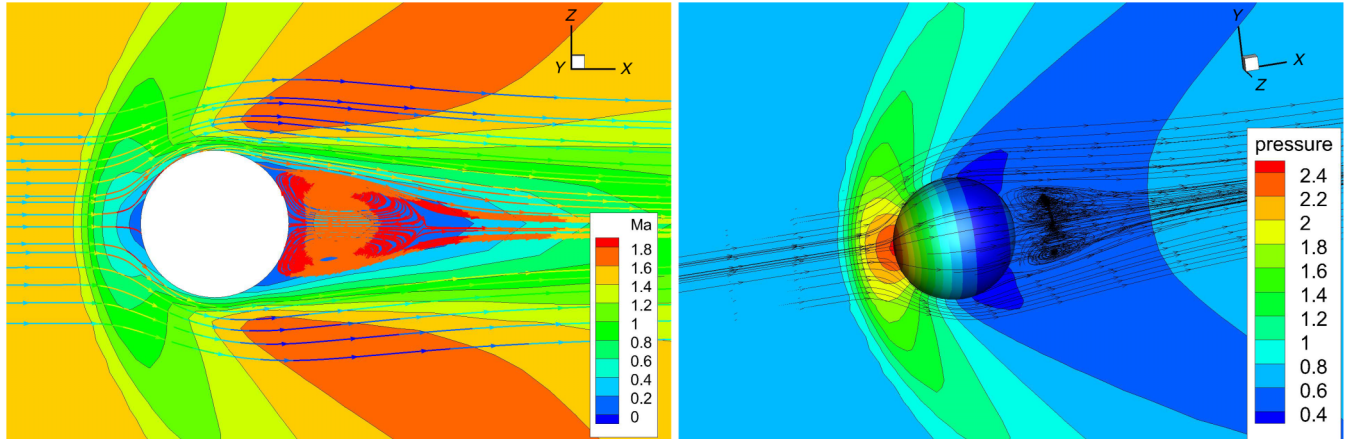


Fig. 17 Supersonic viscous flow passing through a sphere with $Ma = 1.5$ and $Re = 300$. Left: the Mach distributions for the $x$–$z$ planes. The streamline is colored by temperature. Right: the pressure and Mach distributions for the $x$–$y$ and $x$–$z$ planes. The sphere is colored by pressure.
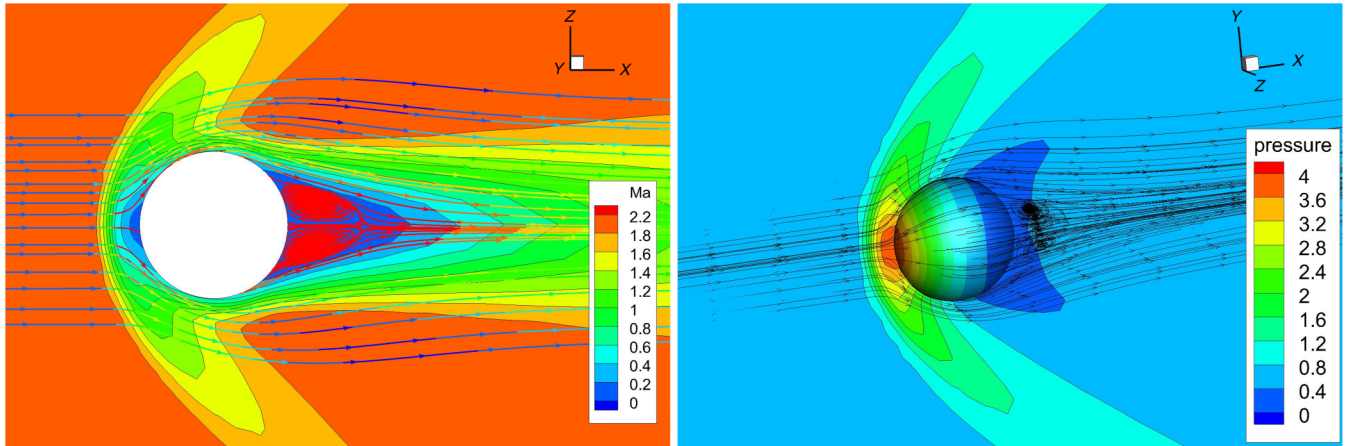
**Fig. 18    Supersonic viscous flow passing through a sphere with $Ma = 2$ and $Re = 300$. Left: the Mach distributions for the $x$–$z$ planes. The streamline is colored by temperature. Right: the pressure and Mach distributions for the $x$–$y$ and $x$–$z$ planes. The sphere is colored by pressure.**

HWENO reconstruction will easily give a negative density or pressure and then reduce to a low-order reconstruction.

For the viscous case, the nonslip adiabatic boundary condition is imposed on the surface of the sphere. The Reynolds number is set as 300 based on the diameter $D$. The Prandtl number is $Pr = 1$. The first grid off the wall is $4.8 \times 10^{-2}D$ with a cell Reynolds number $\approx 14$. The outer domain is around $10D$ in the radial direction. The total cell number is $16 \times 16 \times 32 \times 6 = 49,152$. Two Mach numbers, $Ma = 1.5$ and $Ma = 2$, are tested. The numerical results are shown in Figs. 17 and 18, respectively. Quantitatively comparisons with the reference results given by Nagata et al. [48] on a very fine mesh are listed in Table 5. The $Cd$, $\theta$, and $L$ have the same definition as the subsonic case. The drag coefficients agree nicely with the reference data, even with a much coarse grid.

### F.    Compressible Isentropic Turbulence

A decaying homogeneous isotropic compressible turbulence is computed within a square box defined as $-\pi \leq x, y, z \leq \pi$, and the periodic boundary conditions are used in all directions [49]. A fixed $Re_\lambda = 72$ is investigated in the current work. The random initial

**Table 5    Quantitative comparisons with the reference data for the supersonic viscous flow past a sphere**

| Scheme | $Ma$ | Cell number | $C_d$ | $\theta$ | $L$ |
|---|---|---|---|---|---|
| Sixth-order WENO [48] | 1.5 | 909,072 | 1.370 | 137.2 | 0.96 |
| Current | 1.5 | 49,152 | 1.371 | 139.4 | 0.92 |
| Sixth-order WENO [48] | 2 | 909,072 | 1.386 | 150.9 | 0.38 |
| Current | 2 | 49,152 | 1.345 | 149.5 | 0.5 |

flowfield is determined according to [50]. When $Ma_t = 0.5$, the flow is initially transonic, the maximum Mach number in the flowfield is about three times of the initial turbulent Mach number. The smooth GKS solver (15) and the WENO-AO reconstruction with linear weights can be used under such mild case to achieve a high resolution. Uniform meshes with $64^3$ and $128^3$ cells are used in the simulations. Initially the cell-averaged slopes are constructed automatically by setting the first explicit time step $\Delta t_1 = 0$. The kinetic energy, root-mean-square of density fluctuation, and the skew factor are calculated by

$$K(t) = \frac{1}{2} \ll \rho \boldsymbol{U} \cdot \boldsymbol{U} \gg,$$

$$\rho_{\rm rms}(t) = \sqrt{\ll (\rho - \bar{\rho})^2 \gg},$$

$$S_u(t) = \sum_i \frac{\ll (\partial_i u_i)^3 \gg}{\ll (\partial_i u_i)^2 \gg^{3/2}}$$

Since the cell-averaged $\bar{W}_{x_i}$ is stored in each cell, the $\partial_i u_i$ can be calculated conveniently through the chain rule. The time history of normalized kinetic energy $K(t)/K_0$ and normalized root-mean-square of density fluctuation $\rho_{\rm rms}(t)/Ma_t^2$ agree well with the reference data and the traditional WENO-GKS with $64^3$ cells, as shown in Figs. 19 and 20. For the higher-order moment, the skew factor needs finer meshes to be resolved, as shown in Fig. 21. The CPU times with $128^3$ mesh points on a single core of Intel Xeon E5 2630v4 @2.20 GHz are the following. In each step, the noncompact fifth-order GKS uses 124.9 s, whereas the compact GKS uses 110.6 s.
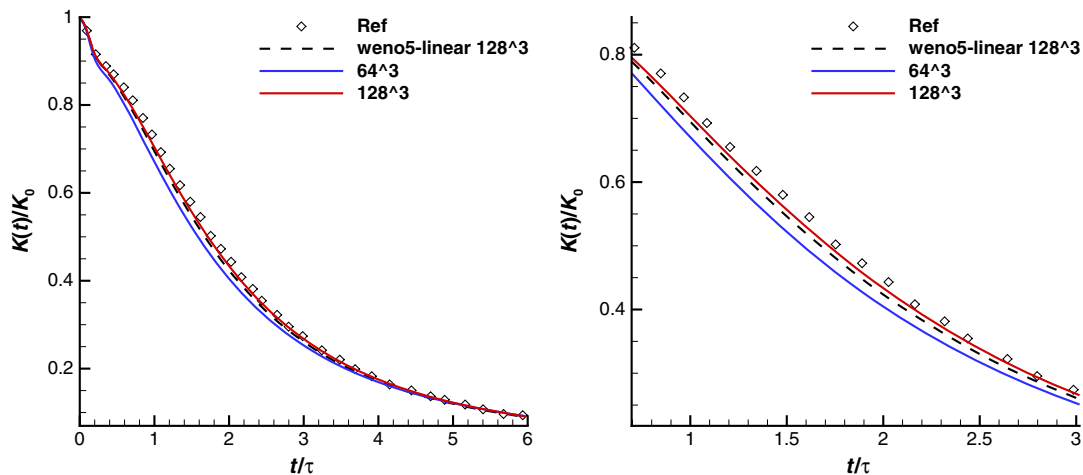


**Fig. 19    Compressible isotropic turbulence: $K(t)/K_0$. $Re_\lambda = 72$, $Ma_t = 0.5$.**
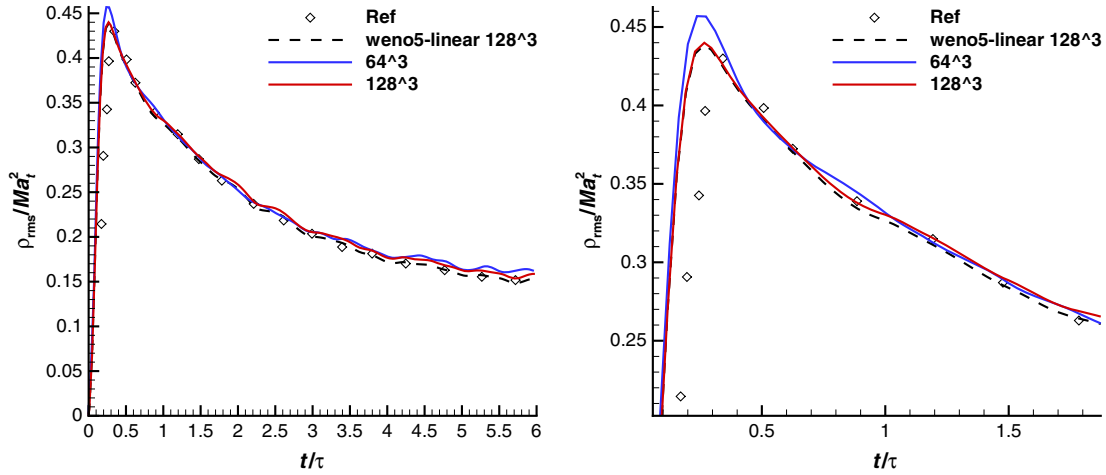
**Fig. 20   Compressible isotropic turbulence: $\rho_{rms}(t)/Ma_t^2$. $Re_\lambda = 72$, $Ma_t = 0.5$.**
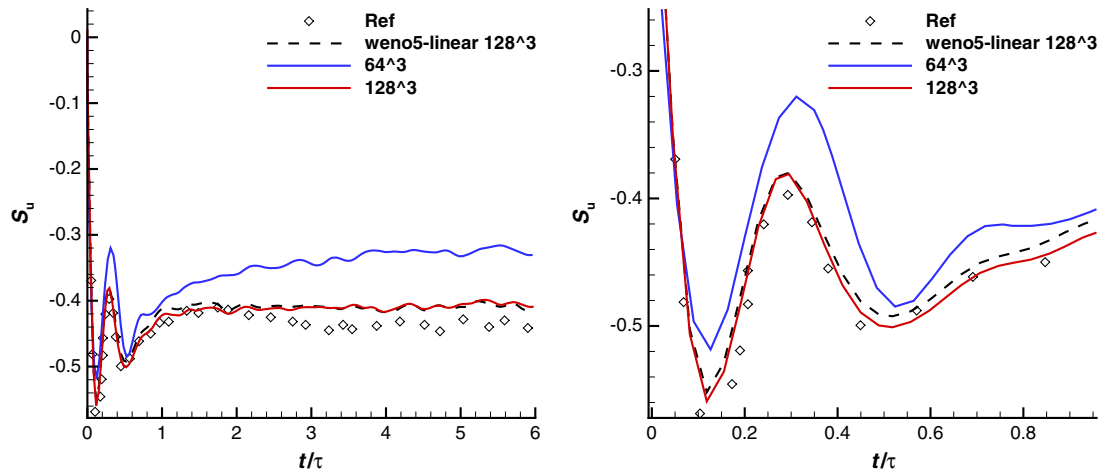


**Fig. 21   Compressible isotropic turbulence: $S_u(t)$. $Re_\lambda = 72$, $Ma_t = 0.5$.**

When the Mach number gets higher, the flow becomes supersonic, and the stronger shocklets are generated, followed by complex shock–vortex interactions. It is nontrivial for high-order methods to survive under $Ma_t \geq 1$. In addition, it becomes more challenging under a coarse mesh, since the discontinuities become stronger due to the limitation of the mesh resolution. Thus, a series of turbulent Mach numbers have been chosen to test the robustness of the current scheme with the mesh $64^3$. In the computation, the full GKS solver in Eq. (12) and the nonlinear HWENO reconstruction are used.

Considering the large velocity jump in the initial field, a modified $\tau$ is taken as

$$\tau = \frac{\mu}{p} + \sum_1^5 \delta Q \Delta t$$

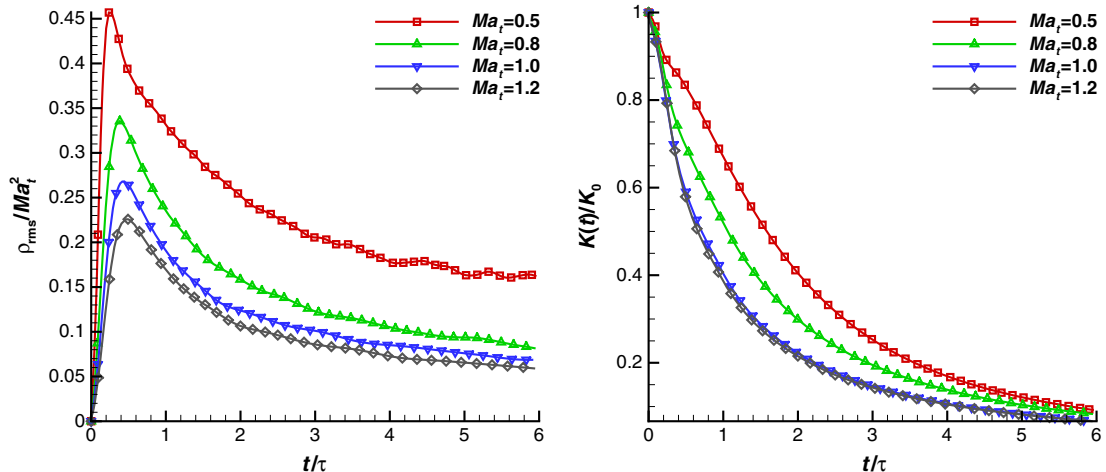where $Q$ means all five primitive variables with



**Fig. 22   Compressible isotropic turbulence: comparison with different $Ma_t$ numbers by the new compact GKS. Mesh: $64^3$. CFL $= 0.5$.**
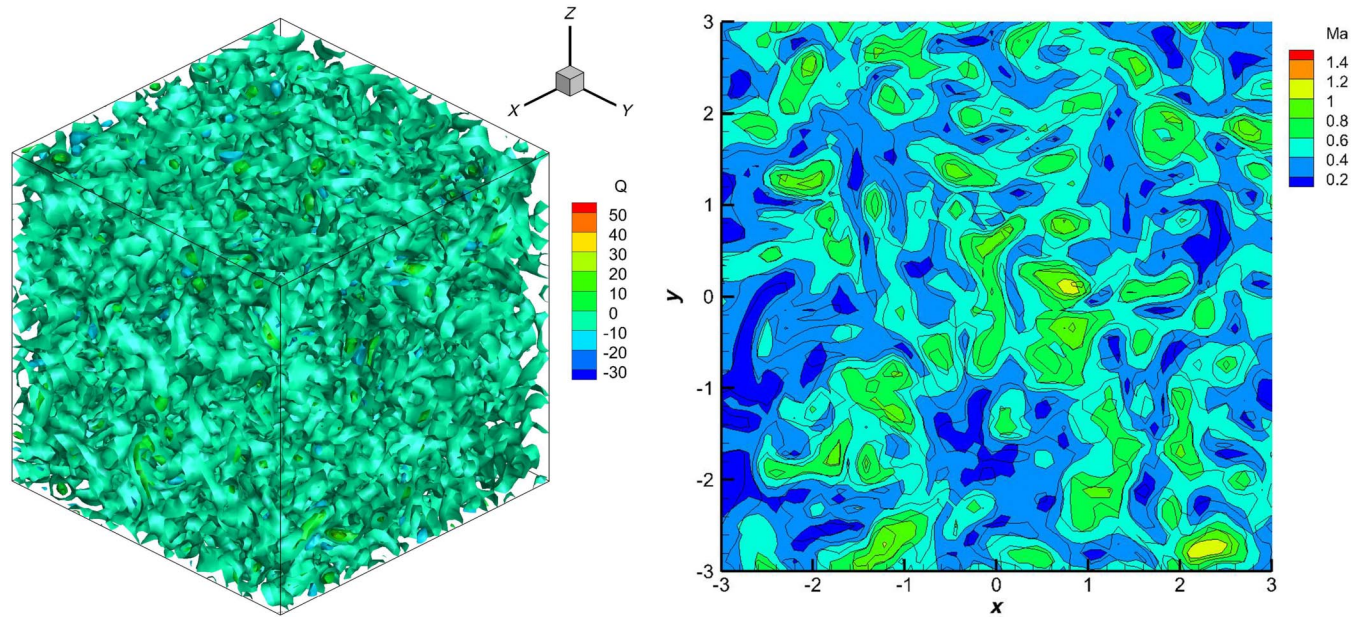
**Fig. 23** **Compressible homogeneous turbulence with $Ma_t = 1$ at $t/\tau_0 = 1$. Left: isosurfaces of $Q$ criterion. Right: Mach number distribution with $z = -\pi$. Mesh: $64^3$.**

$$\delta Q = \frac{|Q^l - Q^r|}{|Q^l| + |Q^r| + 1e^{-10}}$$

The statistical quantities with respect to different Mach numbers are presented in Fig. 22. With the increase of $Ma_t$, the kinetic energy gets dissipated more rapidly. The visualized results, i.e., the isosurfaces of $Q$ criterion colored by Mach number and the selected surface slice of Mach number distribution at $z = -\pi$, are plotted in Fig. 23. The complex vortices and widespread shocklets can be observed clearly.

## VI.    Conclusions

In this paper, a compact high-order gas-kinetic scheme for 3-D flow simulation is presented. The distinguishable feature of the scheme is that the high-order GKS evolution model at a cell interface provides not only the fluxes, but also the time-accurate flow variables. As a result, based on the cell interface values the first-order spatial derivatives of flow variables inside each control volume can be directly obtained through Gauss's theorem at the next time level. The slope update in the current scheme is different from the compact DG-type method, where the weak formulation is used directly for the time evolution of the corresponding degrees of freedom. Consequently, the compact GKS can use a large CFL time step and the scheme is robust in capturing discontinuous solutions without identifying the trouble cells explicitly. To compute the flow with shocks and vortices on nonuniform mesh, a new HWENO reconstruction with less substencils and all positive weights has been designed for the initial data reconstruction in the scheme. At the same time, the two-stage time discretization is used as a time-marching strategy in the scheme, which subsequently leads to a high efficiency in comparison with the traditional RK method for the same temporal accuracy. The compact third-order GKS in 3-D shows similar resolution as the fifth-order gas-kinetic scheme with the noncompact WENO reconstruction. Overall, the time-accurate evolution model, the HWENO reconstruction, and the two-stage time marching technique make the final scheme accurate, robust, and efficient for the compressible flow simulations with smooth and discontinuous solutions. Although the current scheme is constructed on structured mesh, it can be directly extended to unstructured one. The compact third-order and fourth-order HGKS on 3-D unstructured mesh is on the development, which further enlarges the applicable regime of the high-order gas-kinetic schemes for flow computation with complex geometry.

The development of high-order compact GKS with implicit and other acceleration techniques is on the investigation as well for the steady-state solution.

At the end, the similarities and differences of the current compact GKS and the popular $DG/\text{rDG}/P_N P_M$ methods are summarized as follows:

1) *Spatial discretization:* The current compact GKS has the same reconstruction stencil as the rDG-$P_1 P_2$ method [13]. In each cell, the flow variables and their slopes are stored for reconstruction. Thus, the current scheme has the same compactness as the third-order rDG-$P_1 P_2$ scheme, but with different reconstructions.

2) *Solvers:* High-order moments are evolved based on the weak solutions in DG and rDG methods. The corresponding volume integrals are needed to be calculated numerically. The time-independent approximate solvers, such as L-F solver, are used to evaluate the flux at quadrature points. The time step is restricted. For example, the CFL number of the third-order DG is around 0.2 and the CFL number of the rDG-$P_1 P_2$ scheme is around 0.33. However, the cell averaged slopes for the compact GKS are more or less based on the strong solution which is obtained by the time-accurate flow variables at the Gaussian points via the Gauss's theorem analytically. Both the conservative variables and fluxes at cell interfaces are evaluated from the same gas distribution function in Eq. (12) by Eqs. (5) and (6). The volume integral for the slope update is not required in the current method. The compact GKS can use a relatively large CFL number around 0.5 in the computations.

3) *Temporal discretization:* The traditional rDG-$P_1 P_2$ uses the three-stage third-order RK method for temporal discretization [13]. The current compact GKS adopts the S2O4 time discretization, which can provide a temporal accuracy up to fourth order with only two stages. However, the time-dependent gas-kinetic flux is more time-consuming. The two-stage fourth-order building block can also be adopted into the DG or CPR framework, and significant efficiency improvement has been reported [51,52].

4) *Program feasibility:* The current algorithm could be easily developed from a second-order finite volume code, which has the same advantages as the rDG/PnPm methods [12,13].

## Acknowledgment

# References

[1] Shu, C.-W., "High Order Weighted Essentially Nonoscillatory Schemes for Convection Dominated Problems," *SIAM Review*, Vol. 51, No. 1, 2009, pp. 82–126.
https://doi.org/10.1137/070679065

[2] Shu, C.-W., "High Order WENO and DG Methods for Time-Dependent Convection-Dominated PDEs: A Brief Survey of Several Recent Developments," *Journal of Computational Physics*, Vol. 316, July 2016, pp. 598–613.
https://doi.org/10.1016/j.jcp.2016.04.030

[3] Huynh, H. T., "A Flux Reconstruction Approach to High-Order Schemes Including Discontinuous Galerkin Methods," *18th AIAA Computational Fluid Dynamics Conference*, AIAA Paper 2007-4079, 2007.
https://doi.org/10.2514/6.2007-4079

[4] Yu, M., Wang, Z. J., and Liu, Y., "On the Accuracy and Efficiency of Discontinuous Galerkin, Spectral Difference and Correction Procedure via Reconstruction Methods," *Journal of Computational Physics*, Vol. 259, Feb. 2014, pp. 70–95.
https://doi.org/10.1016/j.jcp.2013.11.023

[5] Balsara, D. S., Garain, S., and Shu, C.-W., "An Efficient Class of WENO Schemes with Adaptive Order," *Journal of Computational Physics*, Vol. 326, Dec. 2016, pp. 780–804.
https://doi.org/10.1016/j.jcp.2016.09.009

[6] Zhu, J., and Shu, C.-W., "A New Type of Third-Order Finite Volume Multi-Resolution WENO Schemes on Tetrahedral Meshes," *Journal of Computational Physics*, Vol. 406, April 2020, Paper 109212.
https://doi.org/10.1016/j.jcp.2019.109212

[7] Wang, Z. J., Fidkowski, K., Abgrall, R., Bassi, F., Caraeni, D., Cary, A., Deconinck, H., Hartmann, R., Hillewaert, K., Huynh, H. T., Kroll, N., May, G., Persson, P.-O., van Leer, B., and Visbal, M., "High-Order CFD Methods: Current Status and Perspective," *International Journal for Numerical Methods in Fluids*, Vol. 72, No. 8, 2013, pp. 811–845.
https://doi.org/10.1002/fld.3767

[8] Wang, Z. J., Li, Y., Jia, F., Laskowski, G. M., Kopriva, J., Paliath, U., and Bhaskaran, R., "Towards Industrial Large Eddy Simulation Using the FR/CPR Method," *Computers & Fluids*, Vol. 156, Oct. 2017, pp. 579–589.
https://doi.org/10.1016/j.compfluid.2017.04.026

[9] Yang, X., Cheng, J., Luo, H., and Zhao, Q., "Robust Implicit Direct Discontinuous Galerkin Method for Simulating the Compressible Turbulent Flows," *AIAA Journal*, Vol. 57, No. 3, 2019, pp. 1113–1132.
https://doi.org/10.2514/1.J057172

[10] Qiu, J., and Zhang, Q., "Stability, Error Estimate and Limiters of Discontinuous Galerkin Methods," *Handbook of Numerical Analysis*, Vol. 17, Elsevier, Amsterdam, 2016, pp. 147–171.
https://doi.org/10.1016/bs.hna.2016.06.001

[11] Xie, B., Deng, X., Sun, Z., and Xiao, F., "A Hybrid Pressure–Density-Based Mach Uniform Algorithm for 2D Euler Equations on Unstructured Grids by Using Multi-Moment Finite Volume Method," *Journal of Computational Physics*, Vol. 335, April 2017, pp. 637–663.
https://doi.org/10.1016/j.jcp.2017.01.043

[12] Dumbser, M., "Arbitrary High Order PNPM Schemes on Unstructured Meshes for the Compressible Navier–Stokes Equations," *Computers & Fluids*, Vol. 39, No. 1, 2010, pp. 60–76.
https://doi.org/10.1016/j.compfluid.2009.07.003

[13] Luo, H., Luo, L., Nourgaliev, R., Mousseau, V. A., and Dinh, N., "A Reconstructed Discontinuous Galerkin Method for the Compressible Navier–Stokes Equations on Arbitrary Grids," *Journal of Computational Physics*, Vol. 229, No. 19, 2010, pp. 6961–6978.
https://doi.org/10.1016/j.jcp.2010.05.033

[14] Yang, X., Cheng, J., Liu, X., Wang, C., Si, J., and Luo, H., "A Reconstructed Direct Discontinuous Galerkin Method for Compressible Turbulent Flows on Hybrid Grids," *46th AIAA Fluid Dynamics Conference*, AIAA Paper 2016-3332, 2016.
https://doi.org/10.2514/6.2016-3332

[15] Pan, L., and Xu, K., "A Third-Order Compact Gas-Kinetic Scheme on Unstructured Meshes for Compressible Navier–Stokes Solutions," *Journal of Computational Physics*, Vol. 318, Aug. 2016, pp. 327–348.
https://doi.org/10.1016/j.jcp.2016.05.012

[16] Li, J., and Du, Z., "A Two-Stage Fourth Order Time-Accurate Discretization for Lax–Wendroff Type Flow Solvers I. Hyperbolic Conservation Laws," *SIAM Journal on Scientific Computing*, Vol. 38, No. 5, 2016, pp. A3046–A3069.
https://doi.org/10.1137/15M1052512

[17] Du, Z., and Li, J., "A Hermite WENO Reconstruction for Fourth Order Temporal Accurate Schemes Based on the GRP Solver for Hyperbolic Conservation Laws," *Journal of Computational Physics*, Vol. 355, Feb. 2018, pp. 385–396.
https://doi.org/10.1016/j.jcp.2017.11.023

[18] Qiu, J., and Shu, C.-W., "Hermite WENO Schemes and their Application as Limiters for Runge–Kutta Discontinuous Galerkin Method: One-Dimensional Case," *Journal of Computational Physics*, Vol. 193, No. 1, 2004, pp. 115–135.
https://doi.org/10.1016/j.jcp.2003.07.026

[19] Ji, X., Pan, L., Shyy, W., and Xu, K., "A Compact Fourth-Order Gas-Kinetic Scheme for the Euler and Navier-Stokes Equations," *Journal of Computational Physics*, Vol. 372, Nov. 2018, pp. 446–472.
https://doi.org/10.1016/j.jcp.2018.06.034

[20] Pan, L., Xu, K., Li, Q., and Li, J., "An Efficient and Accurate Two-Stage Fourth-Order Gas-Kinetic Scheme for the Euler and Navier–Stokes Equations," *Journal of Computational Physics*, Vol. 326, Dec. 2016, pp. 197–221.
https://doi.org/10.1016/j.jcp.2016.08.054

[21] Xu, K., "A Gas-Kinetic BGK Scheme for the Navier–Stokes Equations and Its Connection with Artificial Dissipation and Godunov Method," *Journal of Computational Physics*, Vol. 171, No. 1, 2001, pp. 289–335.
https://doi.org/10.1006/jcph.2001.6790

[22] Xu, K., Mao, M., and Tang, L., "A Multidimensional Gas-Kinetic BGK Scheme for Hypersonic Viscous Flow," *Journal of Computational Physics*, Vol. 203, No. 2, 2005, pp. 405–421.
https://doi.org/10.1016/j.jcp.2004.09.001

[23] Gottlieb, S., Shu, C.-W., and Tadmor, E., "Strong Stability-Preserving High-Order Time Discretization Methods," *SIAM Review*, Vol. 43, No. 1, 2001, pp. 89–112.
https://doi.org/10.1137/S003614450036757X

[24] Ji, X., and Xu, K., "Performance Enhancement for High-Order Gas-Kinetic Scheme Based on WENO-Adaptive-Order Reconstruction," *Communications in Computational Physics*, Vol. 28, No. 2, 2020, pp. 539–590.
https://doi.org/10.4208/cicp.OA-2019-0082

[25] Zhao, F., Ji, X., Shyy, W., and Xu, K., "Compact Higher-Order Gas-Kinetic Schemes with Spectral-Like Resolution for Compressible Flow Simulations," *Advances in Aerodynamics*, Vol. 1, No. 1, 2019, p. 13.
https://doi.org/10.1186/s42774-019-0015-6

[26] Zhao, F., Ji, X., Shyy, W., and Xu, K., "An Acoustic and Shock Wave Capturing Compact High-Order Gas-Kinetic Scheme with Spectral-Like Resolution," *International Journal of Computational Fluid Dynamics*, Vol. 34, No. 10, 2020, pp. 731–756.
https://doi.org/10.1080/10618562.2020.1821879

[27] Ji, X., Zhao, F., Shyy, W., and Xu, K., "A HWENO Reconstruction Based High-Order Compact Gas-kinetic Scheme on Unstructured Mesh," *Journal of Computational Physics*, Vol. 410, June 2020, Paper 109367.
https://doi.org/10.1016/j.jcp.2020.109367

[28] Ji, X., Zhao, F., Shyy, W., and Xu, K., "A Family of High-Order Gas-Kinetic Schemes and Its Comparison with Riemann Solver Based High-Order Methods," *Journal of Computational Physics*, Vol. 356, March 2018, pp. 150–173.
https://doi.org/10.1016/j.jcp.2017.11.036

[29] Jiang, G.-S., and Shu, C.-W., "Efficient Implementation of Weighted ENO Schemes," *Journal of Computational Physics*, Vol. 126, No. 1, 1996, pp. 202–228.
https://doi.org/10.1006/jcph.1996.0130

[30] Zhao, F., Pan, L., and Wang, S., "Weighted Essentially Non-Oscillatory Scheme on Unstructured Quadrilateral and Triangular Meshes for Hyperbolic Conservation Laws," *Journal of Computational Physics*, Vol. 374, Dec. 2018, pp. 605–624.
https://doi.org/10.1016/j.jcp.2018.08.008

[31] Zhu, J., and Qiu, J., "A New Third Order Finite Volume Weighted Essentially Non-Oscillatory Scheme on Tetrahedral Meshes," *Journal of Computational Physics*, Vol. 349, Nov. 2017, pp. 220–232.
https://doi.org/10.1016/j.jcp.2017.08.021

[32] Bhatnagar, P. L., Gross, E. P., and Krook, M., "A Model for Collision Processes in Gases. I. Small Amplitude Processes in Charged and Neutral One-Component Systems," *Physical Review*, Vol. 94, No. 3, 1954, p. 511.
https://doi.org/10.1103/PhysRev.94.511

[33] Xu, K., *Direct Modeling for Computational Fluid Dynamics: Construction and Application of Unified Gas-Kinetic Schemes*, World Scientific, Singapore, 2015.
https://doi.org/10.1142/9789814623728_0009

[34] Pan, L., and Xu, K., "High-Order Gas-Kinetic Scheme with Three-Dimensional WENO Reconstruction for the Euler and Navier-Stokes Solutions," *Computers & Fluids*, Vol. 198, Feb. 2020, Paper 104401.
https://doi.org/10.1016/j.compfluid.2019.104401

[35] Li, W., *Efficient Implementation of High-Order Accurate Numerical Methods on Unstructured Grids*, Springer, Berlin, 2014, p. 148.
https://doi.org/10.1007/978-3-662-43432-1

[36] Zhang, R., Zhang, M., and Shu, C.-W., "On the Order of Accuracy and Numerical Performance of Two Classes of Finite Volume WENO Schemes," *Communications in Computational Physics*, Vol. 9, No. 3, 2011, pp. 807–827.
https://doi.org/10.4208/cicp.291109.080410s

[37] Toro, E. F., "The HLLC Riemann Solver," *Shock Waves*, Vol. 29, No. 8, 2019, pp. 1065–1082.
https://doi.org/10.1007/s00193-019-00912-4

[38] Gottlieb, S., "On High Order Strong Stability Preserving Runge–Kutta and Multi Step Time Discretizations," *Journal of Scientific Computing*, Vol. 25, No. 1, 2005, pp. 105–128.
https://doi.org/10.1007/s10915-004-4635-5

[39] Krivodonova, L., and Berger, M., "High-Order Accurate Implementation of Solid Wall Boundary Conditions in Curved Geometries," *Journal of Computational Physics*, Vol. 211, No. 2, 2006, pp. 492–512.
https://doi.org/10.1016/j.jcp.2005.05.029

[40] Luo, H., Baum, J. D., and Löhner, R., "On the Computation of Steady-State Compressible Flows Using a Discontinuous Galerkin Method," *International Journal for Numerical Methods in Engineering*, Vol. 73, No. 5, 2008, pp. 597–623.
https://doi.org/10.1002/nme.2081

[41] Wang, Q., Ren, Y.-X., and Li, W., "Compact High Order Finite Volume Method on Unstructured Grids II: Extension to Two-Dimensional Euler Equations," *Journal of Computational Physics*, Vol. 314, June 2016, pp. 883–908.
https://doi.org/10.1016/j.jcp.2016.03.048

[42] Taneda, S., "Experimental Investigation of the Wake Behind a Sphere at Low Reynolds Numbers," *Journal of the Physical Society of Japan*, Vol. 11, No. 10, 1956, pp. 1104–1108.
https://doi.org/10.1143/JPSJ.11.1104

[43] Cheng, J., Liu, X., Liu, T., and Luo, H., "A Parallel, High-Order Direct Discontinuous Galerkin Method for the Navier-Stokes Equations on 3D Hybrid Grids," *Communications in Computational Physics*, Vol. 21, No. 5, 2017, p. 1231–1257.
https://doi.org/10.4208/cicp.OA-2016-0090

[44] Wang, Q., "Compact High-Order Finite Volume Method on Unstructured Grids," Ph.D. Thesis, Tsinghua Univ., Beijing, 2017.

[45] Pan, J., Wang, Q., Zhang, Y., and Ren, Y., "High-Order Compact Finite Volume Methods on Unstructured Grids with Adaptive Mesh Refinement for Solving Inviscid and Viscous Flows," *Chinese Journal of Aeronautics*, Vol. 31, No. 9, 2018, pp. 1829–1841.
https://doi.org/10.1016/j.cja.2018.06.018

[46] Sun, Y., Wang, Z. J., and Liu, Y., "High-Order Multidomain Spectral Difference Method for the Navier-Stokes Equations on Unstructured Hexahedral Grids," *Communications in Computational Physics*, Vol. 2, No. 2, 2007, pp. 310–333.
https://doi.org/10.2514/6.2006-301

[47] DeBonis, J., "Solutions of the Taylor-Green Vortex Problem Using High-Resolution Explicit Finite Difference Methods," *51st AIAA Aerospace Sciences Meeting Including the New Horizons Forum and Aerospace Exposition*, AIAA Paper 2013-382, 2013.
https://doi.org/10.2514/6.2013-382

[48] Nagata, T., Nonomura, T., Takahashi, S., Mizuno, Y., and Fukuda, K., "Investigation on Subsonic to Supersonic Flow Around a Sphere at Low Reynolds Number of Between 50 and 300 by Direct Numerical Simulation," *Physics of Fluids*, Vol. 28, No. 5, 2016, Paper 056101.
https://doi.org/10.1063/1.4947244

[49] Samtaney, R., Pullin, D. I., and Kosović, B., "Direct Numerical Simulation of Decaying Compressible Turbulence and Shocklet Statistics," *Physics of Fluids*, Vol. 13, No. 5, 2001, pp. 1415–1430.
https://doi.org/10.1063/1.1355682

[50] Cao, G., Pan, L., and Xu, K., "Three Dimensional High-Order Gas-Kinetic Scheme for Supersonic Isotropic Turbulence I: Criterion for Direct Numerical Simulation," *Computers & Fluids*, Vol. 192, Oct. 2019, Paper 104273.
https://doi.org/10.1016/j.compfluid.2019.104273

[51] Cheng, J., Du, Z., Lei, X., Wang, Y., and Li, J., "A Two-Stage Fourth-Order Discontinuous Galerkin Method Based on the GRP Solver for the Compressible Euler Equations," *Computers & Fluids*, Vol. 181, March 2019, pp. 248–258.
https://doi.org/10.1016/j.compfluid.2019.01.025

[52] Zhang, C., Li, Q., Wang, Z., Li, J., and Fu, S., "A Two-Stage Fourth-Order Gas-Kinetic CPR Method for the Navier-Stokes Equations on Triangular Meshes," arXiv preprint arXiv:2010.08914, 2020.

S. Fu
*Associate Editor*